UNIVERSITÀ DELLA CALABRIA

Dipartimento di Ingegneria Informatica, Modellistica, Elettronica e Sistemistica (DIMES)

**Scuola di Dottorato**

Archimide

**Indirizzo**

Science, Comunicazione e Tecnologie

**CICLO**

XXVIII

**TITOLO TESI**

*A Defect-Centric Analysis of the Channel Hot Carrier Degradation*

**Settore Scientifico Disciplinare** ING-INF/01

**Direttore:** Ch.mo Prof. Pietro Pantano

Firma ______________________________

**Supervisori:** Ch.mo Prof. Felice Crupi

Firma ______________________________

**Dottorando:** Luis-Miguel Prócel-Moya

Firma ______________________________

*Para Jeanina*
*por todo su amor, apoyo y paciencia...*

# Acknowledgments

I would like to show my gratitude to Prof. Felice Crupi for his supervising, his help and his advices during my studies at the UNICAL. I learned a lot during our technical discussions.

I would like to thank Prof. Giuseppe Cocorullo, Prof. Marco Lanuzza, Prof. Pasquale Corsonello, Prof. Stefania Perri and Prof. Gregorio Cappuccino for all the lessons learned at the NML laboratory.

I would like to show my gratitude to USFQ and its authorities: Carlos Montúfar, Ximena Córdova, Santiago Gangotena and César Zambrano for their economical support during this program.

I would also like to thank Prof. Lionel Trojman, for his great discussions, lessons and new measure techniques learned at USFQ.

I would like to show special thanks to the people from Imec: Jacopo Franco and Ben Kaczer for their invaluable research collaboration.

Finally, I would like to thank all my colleagues at the NML lab: Paúl, Marco, Noemi, Vincenzo, Sebastiano, Ramiro, Lorena and Domenico for all the great moments we have had during my studies.

# Sommario

Durante l'ultimo decennio, il *channel hot carrier* (CHC) é stato considerato uno dei più importanti meccanismi di degrado della moderna tecnologia CMOS. La degradazione CHC si verifica quando un voltaggio superiore a quello di saturazione viene applicato sul terminale di *drain* e, contemporaneamente, un voltaggio superiore alla tensione di soglia ($V_{TH}$) viene applicato sul terminale di *gate*. Nel presente lavoro, abbiamo utilizzato la cosiddetta *defect-centric distribution* (DCD) per spiegare e descrivere il meccanismo di degradazione CHC. Il DCD si basa su due presupposti: il $V_{TH}$ prodotto da una singola carica segue una distribuzione esponenziale (valore medio $\eta$) e il numero totale di difetti segue la distribuzione di Poisson (valore medio $N_t$). La combinazione di questi due presupposti da come risultato la DCD. Negli ultimi anni, la distribuzione DCD è stata usata per descrivere e spiegare la *bias temperature instability* (BTI) ed è in grado di predirre le code estreme della distribuzione $\Delta V_{TH}$ fino a $4\sigma$. Il vantaggio di usare il DCD è che i suoi primi e secondi momenti sono direttamente correlati ai parametri fisici $\eta$ e $N_t$.

Nel presente lavoro, é stato dimostrato che il DCD è anche in grado di descrivere e spiegare il degrado della distribuzione $\Delta V_{TH}$ fino a $3\sigma$. É stata studiata la dipendenza dei parametri *deffect-centric*, $\eta$ e $N_t$, in relazione alla geometria del dispositivo. É stato dimostrato che $\eta$ è inversamente proporzionale all'area del dispositivo come in la degradazione BTI. Inoltre, il valore previsto della distribuzione $\Delta V_{TH}$ $(<\Delta V_{TH}>)$ si incrementa fortemente quando la lunghezza di canale ($L$) diminuisce e si incrementa debolmente con il decremento della larghezza del dispositivo ($W$). In la degradazione BTI, si riporta che non vi è alcuna dipendenza tra $<\Delta V_{TH}>$ ed $L$. Pertanto, la forte dipendenza trovata è da atribuire alla degradazione CHC. Si é anche studiata la dipendenza della temperatura ($T$) dei parametri *defect-centric* e abbiamo trovato che $\eta$ non dipende da $T$, al contrario degli esperimenti BTI, dove invece $N_t$ aumenta con $T$, fatto che si spiega con l'attivazione del meccanismo di dispersione elettrone-elettrone. Inoltre, abbiamo estratto una energia di attivazione di $\sim 56meV$ per $N_t$. Finalmente, abbiamo usato dispositivi *matching-pair* con la finalitá di studiare la variabilità tempo zero e la variabilità dipendente dal tempo. É stato dimostrato che il tempo di stress e la tensione di stress applicati sul terminale di *drain* non influenzano la variabilità.

# Summary

During the last decade, channel hot carrier (CHC) has been considered one of the most important degradation mechanisms in modern CMOS technology. The CHC degradation occurs when a voltage higher than the saturation voltage is applied on the drain terminal and, simultaneously, a voltage higher than the threshold voltage ($V_{TH}$) is applied on the gate terminal. In the present work, we have used the so-called defect-centric distribution (DCD) in order to explain and describe the CHC degradation mechanism. The DCD is based in two assumptions: the $V_{TH}$ produced by a single charge follows an exponential distribution (mean value $\eta$) and the total number of traps (or defects) is Poisson distributed (mean value $N_t$). The combination of these two assumptions gives us the DCD. During the last years, the DCD distribution has been used for describing and explaining the bias temperature instability (BTI) and it is able to predict the extreme tails of the $V_{TH}$ shift distribution up to $4\sigma$. The advantage of using the DCD is that its first and second moments are directly related to the physical parameters $\eta$ and $N_t$.

In our work, we have shown that the DCD is also able to describe and explain the $V_{TH}$ shift distribution of CHC degradation up to $3\sigma$. We have studied the dependence of the defect-centric parameters , $\eta$ and $N_t$, with respect to the device geometry. We have shown that $\eta$ is inversely proportional to the device area as in BTI degradation. As well, the expected value of the $V_{TH}$ shift distribution ($< \Delta V_{TH} >$) strongly increases when the channel length ($L$) decreases and weakly increases with the decrement of the device width ($W$). In BTI degradation, it has been reported that there is no dependence between $< \Delta V_{TH} >$ and $L$; therefore, the strong dependence we have found is the *signature of the CHC degradation*. As well, we have studied the temperature ($T$) dependence of the defect centric parameters and we have found that $\eta$ does not depend on $T$, as in BTI experiments, whereas $N_t$ increases with $T$, which is explained by the activation of the electron-electron scattering mechanism. Moreover, we have extracted an activation energy of $\sim 56meV$ for $N_t$. Finally, we have used matching pair devices in order to study the time-zero variability and the time-dependent variability. We have shown that the stress time and the stress voltage applied on the drain terminal do not affect the time-dependent variability.

# List of Publications

**Journal Papers:**

1. **L. M. Prócel**, F. Crupi, J. Franco, L. Trojman, B. Kaczer. *A Defect-Centric Analysis of the Temperature Dependence of the Channel Hot Carrier Degradation in nMOSFETs.* submitted to IEEE Transactions on Device and Materials Reliability.

2. **L. M. Prócel**, F. Crupi, J. Franco, L. Trojman, B. Kaczer, N. Wils, H. Tuinhout. *A Defect-Centric perspective on channel hot carrier variability in nMOSFETs.* Microelectronic Engineering, vol. 147, pp. 72-74, 2015.

3. **L. M. Prócel**, F. Crupi, J. Franco, L. Trojman, B. Kaczer. *Defect-Centric Distribution of Channel Hot Carrier Degradation in Nano-MOSFETs.* IEEE Electrron Device Letters, vol. 35, pp. 1167-1169, 2014.

4. **L. M. Prócel**, L. Trojman, J. Moreno, F. Crupi, V. Maccaronio, R. Degraeve, L. Goux, E. Simoen. *Experimental evidence of the Quantum Point Contact theory in the conduction mechanism of bipolar HfO2-based resistive Ran-*

*dom Access Memories.* Journal of Applied Physics, vol. 114, pp. 074509, 2013.

5. V. Maccaronio, F. Crupi, **L. M. Prócel**, L. Goux, E. Simoen, L. Trojman, E. Miranda. *DC and low-frequency noise behavior of the conductive filament in bipolar HfO2-based Resistive Random Access Memory.* Microelectronic Engineering, vol. 107, pp.1-5, 2013.

6. L. Villamagua, R. Barreto, **L. M. Prócel**, A. Stashans. *Hydrogen impurity in SrTiO3: structure, electronic properties and migration.* Physica Scripta, vol. 75, pp. 374-378, 2007.

7. C. Zambrano, A. Sánchez, **L. M. Prócel**, A. Stashans. *Structural and electronic properties of PbZrxTi1-xO3 (x=0.5, 0.375): a quantum-chemical study.* Internacional Journal of quantum Chemistry, vol. 95, pp. 37, 2003.

8. **L. M. Prócel**, F. Tipán, A. Stashans. *Mott-Wannier excitons in the tetragonal BaTiO3 lattice.* International Journal of Quantum Chemistry, vol. 91, pp. 586, 2003.

9. Stashans, C. Zambrano, A. Sánchez, **L. M. Prócel**. *Structural properties of PbTiO3 and PbZrxTi1-xO3: a quantum-*

*chemical study.* International Journal of Quantum Chemistry, vol. 87, pp. 145-151, 2002.

**Conference Papers:**

1. B. Kaczer, J. Franco, M. Cho, T. Grasser, Ph. J. Roussel, S. Tyaginov, M. Bina, Y. Wimmer, **L. M. Procel**, L. Trojman, F. Crupi, G. Pitner, V. Putcha, P. Weckx, E. Bury, Z. Ji, A. De Keersgieter, T. Chiarella, N. Horiguchi, G. Groeseneken, A. Thean. *Origins and implications of increased channel hot carrier variability in nFinFETs*, presented at IEEE International Reliability Physics Symposium (IRPS), pp. 3B.5.1 - 3B.5.6, 2015.

2. R. Viteri, **L. M. Prócel**, F. Tipán, D. F. Ortiz, *A. Stashans. Quantum-chemical study of excitons in tetragonal BaTiO3 and SrTiO3 crystals*, presented at SPIE Proceedings, vol. 5122, pp. 295-302, 2003.

3. A. Sánchez, C. Zambrano, **L. M. Prócel**, A. Stashans. *Structural and electronic properties of PZT*, presented at SPIE Proceedings, vol. 5122, pp. 310-316, 2003.

# Contents

**1 Introduction** **10**

1.1 Channel Hot Carrier degradation in long channel devices . . . 10

1.2 Channel Hot Carrier degradation in short channel devices . . . 12

1.3 Aim of this work: A Defect-Centric Analysis . . 15

1.4 Outline of the document . . . 17

**2 Principal Channel Hot Carrier Degradation Models in Short Devices** **18**

2.1 Hess model . . . 19

2.2 Rauch and La Rosa model (energy driven paradigm model) . . . 23

2.3 Bravaix model . . . 25

2.4 Tyaginov and Bina model . . . . . . . . . . . . . 29

**3 Experimental and Analytical Tools for Studying the Channel Hot Carrier Degradation under the Defect-Centric Point of View 34**

3.1 Principal channel hot carrier measurement techniques . . . . . . . . . . . . . . . . . . . . . . . 35

3.1.1 I-V stress . . . . . . . . . . . . . . . . . . 35

3.1.2 Measure-Stress-Measure (MSM) technique 36

3.2 The defect-centric distribution . . . . . . . . . . 38

**4 Study of the Geometry Device Dependence of the Defect-Centric Parameters 41**

4.1 Defect-centric distribution of experimental data of CHC-induced $\Delta V_{TH}$ . . . . . . . . . . . . . . . 42

4.2 Length and width dependences of the defect-centric parameters . . . . . . . . . . . . . . . . . . . . . 46

**5 A Defect-Centric Analysis of the Temperature Dependence of the Channel Hot Carrier Degradation 53**

5.1 Temperature dependence of the defect-centric parameters . . . . . . . . . . . . . . . . . . . . . . . . 54

5.2 Extraction of the activation energy . . . . . . . . 59

**6 A Defect-Centric Study of the Channel Hot Carrier Variability 63**

6.1 Variability concepts . . . . . . . . . . . . . . . . . 64

6.2 Experimental results . . . . . . . . . . . . . . . . . 67

6.2.1 Drain voltage and stress time dependences 68

6.2.2 Time-zero variability . . . . . . . . . . . . . 71

6.2.3 Time-dependent variability . . . . . . . . 73

**7 General Conclusions and Future Work 78**

7.1 Conclusions . . . . . . . . . . . . . . . . . . . . . 78

7.2 Future work . . . . . . . . . . . . . . . . . . . . . 80

**Appendices 81**

**A Activation Energy Conversion 82**

**B Conversion between the Variances of Single Device Experiments and Matching Pairs Experiments 85**

**Bibliography 87**

# List of Figures


2.1 Left: SP and MP mechanisms, which are represented by the truncated harmonic oscillator. Right: schematic of the analogous AB and MVE processes. Figure taken from [4]. . . . . . . . . . . 20

2.2 A sketch of the cross section function ($S(E)$), the carrier energy density function, ($DF(E)$, in the plot $f(E)$), and the product of both function ($DF(E)S(E)$). Figure taken from [4]. . . . . . . 25

3.1 $I_{DS} - V_{GS}$ characteristics for several stress times. We can see that the characteristic curve moves to the right when the stress time increases, showing an increment of $V_{TH}$. In the I-V stress technique, the $V_{TH}$ is extracted from the complete curve. . 36

3.2 An example of a logarithmic stress pulse of the MSM technique. Top: the stress pulse for the gate terminal. Bottom: the stress pulse for the drain terminal. In this case, $V_{Gsense} = 0.5V$ and $V_{Dsense} = 0.05V$. . . . . . . . . . . . . . . . . . . . 37

3.3 In the MSM technique, during the sense time, the $I_{DS}$ current is measured several times according to the logarithmic pulse (square dots). These values are projected into the initial $I_{DS} - V_{GS}$ curve in order to extract the $\Delta V_{TH}$ value. . . . . . . . 38

4.1 Distributions of the CHC-induced $\Delta V_{TH}$ for several stress times. We can see that $\eta$ is constant and the variation of $< \Delta V_{TH} >$ is only due to the increment of $N_t$. In this case: $V_{Gstress} = V_{Dstress} = 2V$. . . . . . . . . . . . . . . . . . . . . . 43

4.2 $N_t$ increases with respect to $t_{stress}$. The exponent of the power law $N_t = t^n$ is 0.45. . . . . . . 44

4.3 CHC-induced $\Delta V_{TH}$ follows a DCD in $45nm$ commercial technology. In this case: $V_{Gstress} = 1.1V$ and $V_{Dstress} = 1.8V$. . . . . . . . . . . . . . . . . . . 45

4.4 CHC-induced $\Delta V_{TH}$ follows a DCD in $65nm$ commercial technology. In this case: $V_{Gstress} = 1.2V$ and $V_{Dstress} = 1.8V$. . . . . . . . . . . . . . . . . . 46
4.5 $\Delta V_{TH}$ for different $L_{eff}$ and same $W = 90nm$. The first and second moments strongly decrease with $L_{eff}$. . . . . . . . . . . . . . . . . . . . . . . . 47
4.6 $\Delta V_{TH}$ for different $W$ and same $L_{eff} = 100nm$. The first and second moments weakly decrease with $W$. . . . . . . . . . . . . . . . . . . . . . . . . 48
4.7 $< \Delta V_{TH} >$ as function of $L_{eff}$ or $W$. The expected value of $\Delta V_{TH}$ strongly decreases with $L_{eff}$ and weakly decreases with $W$. . . . . . . . . 49
4.8 $\eta$ scales as $1/A_{eff}$. . . . . . . . . . . . . . . . . . . 50
4.9 $N_t$ as function of $L_{eff}$ or $W$. $N_t$ decreases with $L_{eff}$ and increases with $W$. . . . . . . . . . . . . 51
4.10 $D_t$ as function of $L_{eff}$ or $W$. $D_t$ strongly decreases with $L_{eff}$ and slightly decreases with $W$. 52

5.1 CHC-induced $\Delta V_{TH}$ distribution for several temperatures. All experiments agree well with the DCD. We can see that $< \Delta V_{TH} >$ increases with $T$. . . . . . . . . . . . . . . . . . . . . . . . . . 55

5.2 The expected value of the CHC induced $V_{TH}$ shift increases with $T$ in agreement to the activation of the EES mechanism. . . . . . . . . . . . . . . 56

5.3 $N_t$ increases as function of $T$. On the right axis, $D_t$ is plotted. . . . . . . . . . . . . . . . . . . . . . 57

5.4 $\eta$ is independent of $T$. . . . . . . . . . . . . . . . 58

5.5 Arrhenius plot of $< \Delta V_{TH} >$ for small and large devices. For both geometries, similar values of $E_{ACT}$ are obtained. . . . . . . . . . . . . . . . . 61

5.6 Arrhenius plot of $N_t$ for several stress times. $E_{ACT}$ values are similar to those obtained for BTI degradation. . . . . . . . . . . . . . . . . . . . . . . . 62

6.1 The expected value of the CHC-induced $\Delta V_{TH}$ follows a power law with respect to $t_{stress}$ with an average slope of $\sim 0.55$ for the $45nm$ technology. 69

6.2 The expected value of the CHC-induced $\Delta V_{TH}$ follows a power law with respect to $t_{stress}$ with an average slope of $\sim 0.55$ for the $65nm$ technology. 69

6.3 The expected value of the CHC-induced $\Delta V_{TH}$ follows a power law with respect to $V_{Dstress}$ with an average slope of $\sim 0.12$ for the $45nm$ technology. 70

6.4 The expected value of the CHC-induced $\Delta V_{TH}$ follows a power law with respect to $V_{Dstress}$ with an average slope of $\sim 0.13$ for the $65nm$ technology. 70
6.5 The time-zero $V_{TH0}$ follows a normal distribution up to $3\sigma$ for both technologies. . . . . . . . . . . 72
6.6 The time-zero mismatch follows a normal distribution up to $3\sigma$ for both technologies. . . . . . . 72
6.7 Total and intrinsic time-zero variabilities in function of the effective channel length for both technologies. . . . . . . . . . . . . . . . . . . . . . . . . 73
6.8 The time-dependent mismatch follows a normal distribution up to $3\sigma$ for several stress times in $45nm$ technology. . . . . . . . . . . . . . . . . . . . 74
6.9 The time-dependent mismatch follows a normal distribution up to $3\sigma$ for several stress times in $65nm$ technology. . . . . . . . . . . . . . . . . . . . 74
6.10 The time-dependent variability is practically independent of the stress time in $45nm$ technology. 76
6.11 The time-dependent variability is practically independent of the stress time in $65nm$ technology. 76
6.12 The time-dependent variability is practically independent of the drain voltage in $45nm$ technology. 77

6.13 The time-dependent variability is practically independent of the drain voltage in $65nm$ technology. 77

A.1 In this simulated plot of $< \Delta V_{TH} >$ vs. $t_{stress}$, we can see the difference between both activation energies. In this case the exponent of the power law is 0.5. . . . . . . . . . . . . . . . . . . . . . . . 84

# Chapter 1

# Introduction

## 1.1 Channel Hot Carrier degradation in long channel devices

During the 80's, the study of the Channel Hot Carrier (CHC) degradation had a lot of interest because of the high voltages (∼5V) applied on the drain and gate terminals when the Metal-oxide-semiconductor field-effect transistor (MOSFET) was in on-state. The application of a gate voltage ($V_{GS}$) larger than the threshold voltage ($V_{TH}$) and, simultaneously, a drain voltage ($V_{DS}$) larger than the saturation voltage provokes the injec-

tion of high energetic electrons and holes (hot carriers) into the gate dielectric. The most accepted physical mechanism for CHC degradation in large devices is that hot carriers are generated by the impact ionization mechanism at the pinch-off region. This mechanism is supported by lucky-electron model developed by Chemin Hu [1, 2, 3]. In this model, a single particle (electron or hole) is accelerated by the lateral electric field ($E_{lat}$) in the channel, and then it collides with a valence electron of a static crystal atom. As result of this collision, an electron-hole pair with enough energy to cross the band gap of the dielectric oxide is generated [1, 2, 3, 4]. With this model, the field-driven paradigm began, since hot carrier are supposed to be generated and controlled by the $E_{lat}$.

Microscopically, this carrier injection provokes a degradation of the oxide-channel interface due to the increment of the interface traps ($\Delta N_{it}$) [4, 5]. Macroscopically, this interface degradation causes a reduction of the drain current ($I_{DS}$) and an increment of $V_{TH}$. In addition, $\Delta N_{it}$ in function of the stress time ($t_{stress}$) follows a power law with a typical exponent of 0.5 [5].

In nMOSFETs, hot electrons are injected into the gate, whereas hot holes are injected into the bulk generating an increment

of the bulk current ($I_{BS}$), which is a measure of the CHC degradation severity [4, 5]. In pMOSFETs occurs the opposite: hot holes are injected into the gate and hot electrons into the bulk. The maximum of $I_{BS}$ is the criterion for considering the maximum CHC degradation (worst-case) and it occurs when $V_{GS} = V_{DS}/2$ [4, 5, 6]. The typical criteria for calculating the transistor life-time are: a reduction of 10% of $I_{DS}$ in the saturation region, a reduction of 10% of $I_{DS}$ in the linear region or a $V_{TH}$ shift of 30mV [6, 7, 8].

## 1.2 Channel Hot Carrier degradation in short channel devices

With the scalings of the channel length and the supply voltage, the CHC degradation was considered less relevant during the 90's, whereas the bias temperature instability degradation (which provokes a $V_{TH}$ shift due to an application of a $V_{GS} > V_{TH}$ at high temperature) became more important [5, 6]. However, the supply voltage scaling slows down in comparison to the channel length scaling due to the non-scalability of the sub threshold slope [6, 7, 9, 10]. This has originated that, from the beginning of the last decade, CHC injection was again con-

sidered one of the most important degradation mechanisms.

When the channel length decreases below the 130nm, the maximum damage condition changes from the maximum impact ionization ($V_{GS} = V_{DS}/2$) to $V_{GS} = V_{DS}$, where a higher vertical electric filed is applied [4, 5, 6, 11]. The exponent of the power law of $\Delta N_{it}$ vs. $t_{stress}$ is still found between 0.4$\sim$0.6 showing that the dominant damage is generated by the increment of $\Delta N_{it}$ [5]. However, in [11], it has been found exponents of the power law in the range 0.1$\sim$0.2 in CHC experiments done in short channel nFinFETS with high-$\kappa$ dielectric, showing, in these cases, that the dominant degradation mechanism is the generation of oxide bulk defects. The peak of $N_{it}$ in function of the channel length coordinate shows the maximum degradation region in the channel, which is located at the drain overlap [4, 5]. However, this peak does not coincide with the maximum of $E_{lat}$ [4].

In short devices, the channel length is not enough to accelerate the charges in order to generate electron-hole pairs with enough energy to cross the dielectric band-gap [4, 5]. In addition, it has been found channel hot carrier degradation even at low stress voltages in short devices [4, 5]. All these evidences show that

in short devices, the $E_{lat}$ is not the only cause of damage to the device. In order to explain these changes, the energy-driven paradigm developed by Rauch and La Rosa was introduced. According to this new paradigm, the carrier energy plays the most important role to damage the oxide-channel interface [12].

It is well known that the increment of $\Delta N_{it}$ is caused by the rupture of the Si-H bond during CHC degradation [4, 5, 13, 15]. This rupture can be done by a single particle (SP, like in the lucky-electron model) or by a series of multiple particles (MP, cold carriers) that bombard the bond until its rupture [4, 5, 13, 14]. In ultra-scaled devices, the probability of having a SP mechanism is very low and the MP mechanism is dominant [4]. A good way to understand the CHC degradation mechanism is by computing the carrier energy density function (DF), which takes into account the majority of the energy exchange mechanisms like: impact ionization, surface scattering, scattering at ionized impurities, electron-phonon scattering, and electron-electron scattering (EES). As well, other important mechanisms like Auger recombination and electron-dipole interaction can be considered [4, 5, 13, 16]. In long devices, the scattering mechanisms depopulate the high energies of the carrier energy DF and then soften the CHC degradation in agreement to the decrement

of this degradation with respect to the temperature ($T$) [17]. On the other hand, in short channel devices, the EES plays an important role and populates the tail of the carrier energy DF, and as result, the increment of $T$ increases the CHC degradation [4, 5, 13, 18].

## 1.3 Aim of this work: A Defect-Centric Analysis

The purpose of this work is to understand the defect generation (microscopical property) from the extraction of the $V_{TH}$ shift (macroscopical property) caused by the CHC degradation. In order to study the defect generation, we use the so-called Defect-Centric theory developed by Kaczer and Graser in [19, 20]. The result of this theory is the Defect-Centric distribution (DFD), which is based in two assumptions [19, 20]:

i) the $V_{TH}$ shift produced by a single charge follows an exponential distribution with mean value $\eta$, and

ii) the total number of traps follows a Poisson distribution with mean value $N_t$.

The DCD has been used for describing and explaining the

BTI degradation behaviour, and it has been shown that it can predict very well the extreme tails of the $V_{TH}$ shift distribution up to $4\sigma$ [22]. The DCD and its capacity of predicting the BTI behaviour has been tested in five generations of Intel technologies (from $90nm$ to $22nm$) in different materials and architectures, showing very good results [23]. The model takes into account the traps located in the oxide as well as the interface traps without any distinction [21].

The average parameters used for estimating the life-time in long devices (see section 1.1) are not valid in short devices where the complete distribution is needed to understand and predict the degradation behaviour [19, 20]. The principal reason is that only few atomistic defects can affect the device operation behaviour in ultra-scaled devices. In addition, there is a limited number of studies on the statistical distribution of CHC-induced degradation in nanoscale devices [24, 25, 26, 27]. Taking into account all these considerations, the novelty of the present work is to use the Defect-Centric model (used and tested in BTI degradation) in order to explain the CHC degradation behaviour. This type of analysis is extremely useful to physically understand the CHC degradation of nanoscale MOSFETs in terms of individual defects.

## 1.4 Outline of the document

Chapter 2: The principal physical models for explaing the CHC degradation are reviewed in this chapter. Here, we study the Hess model, the energy-driven paradigm, the Bravaix model and the Tyaginov model.

Chapter 3: Here, we present the principal experimental measurement techniques. In addition, a complete description of the DCD is presented.

Chapter 4: In this chapter, we show a defect-centric analysis of the CHC degradation for different geometries. As well, the principal defect-centric parameter dependences are studied.

Chapter 5: Here, we present a Defect-Centric analysis of the temperature dependence in CHC degradation.

Chapter 6: This chapter shows a defect-centric analysis of the time-zero variability and the time-dependent variability.

Chapter 7: Finally, conclusions and future works are presented in this chapter.

# Chapter 2

# Principal Channel Hot Carrier Degradation Models in Short Devices

The four principal models used for explaining the CHC degradation in short devices are described in this chapter. A very good review of these models can be found in [4]. All these models emerged from the necessity of explaining and understanding the CHC degradation in short devices, where the field-driven paradigm is not longer valid.

## 2.1 Hess model

Originally, this model was developed to understand and simulate the absorption and desorption processes of the hydrogen/deuterium from passivated Si interfaces [30, 31, 32]. The main contribution of this model is the introduction of the acceleration integral (AI). As we explained before, the peak of $\Delta N_{it}$ does not coincide with the $E_{lat,max}$, either with other macroscopical quantities, such as the average carrier density and dynamic temperature [4, 28, 29]. The behaviour of the $\Delta N_{it}$ peak is better explained by the AI, *which represents the cumulative ability to dissociate bonds* [4]. The Hess model introduces the use of the AI for representing the SP and MP mechanisms. The bond rupture process provoked by a single particle is caused by the excitation of bonding electrons to an antibonding state; therefore, a repulsive force is induced over the H atom, generating its release [4]. This mechanism is called AB process, whose AI has the form [4, 30, 31, 32] (see Fig. 2.1).

$$R_{SP} \sim \int_{E_{TH}}^{\infty} F(E)P(E)\sigma(E)dE, \qquad (2.1)$$

where $R_{SP}$ is the SP rate, $F(E)$ is the carrier flux, $\sigma(E)$ is the bond dissociation reaction cross section, $P(E)$ is the proba-

bility of such reaction releases a H atom, and $E_{TH}$ is the bond-breakage energy for this reaction. The carrier flux is the number of charges impinging the interface per unit area, per time, and per unit energy, and it is the result of:

$$F(E) = f(E)g(E)v(E) = DF(E)v(E), \tag{2.2}$$

where $f(E)$ is the carrier distribution probability, $g(E)$ is the density-of-states (DOS), $v(E)$ is the carrier velocity, and $DF(E)$ is the carrier energy DF.

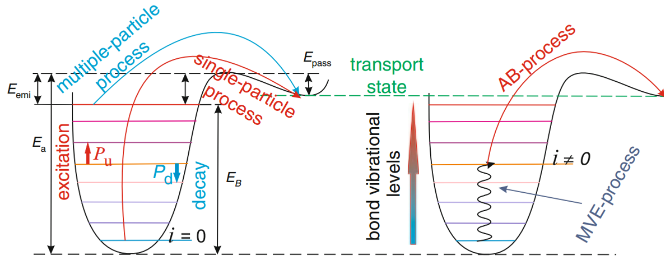


**Figure 2.1:** Left: SP and MP mechanisms, which are represented by the truncated harmonic oscillator. Right: schematic of the analogous AB and MVE processes. Figure taken from [4].

The Hess model also introduce the concept of the multiple vibrational excitation (MVE) of the bond associated to the MP

mechanism (see Fig. 2.1). This process is triggered when a series of cold carriers excite the electron bond until its rupture. The AIs of the MVE process are related to the rates of excitation ($P_u$) and deexcitation ($P_d$) processes, which are explained by the truncated harmonic oscillator model for representing the Si-H bond (see Fig. 2.1). These AIs have the following expressions [4]:

$$P_d \sim \int_{E_{TH}}^{\infty} I(E)\sigma_{ab}(E)\left(1 - f_{ph}(E - \hbar\omega)\right) dE, \tag{2.3}$$

$$P_u \sim \int_{E_{TH}}^{\infty} I(E)\sigma_{emi}(E)\left(1 - f_{ph}(E - \hbar\omega)\right) dE, \tag{2.4}$$

where $I(E)$ is the carrier flux bombarding the bond, $\sigma_{ab}$ and $\sigma_{emi}$ are the cross sections for the phonon absorption and emission reactions, and $f_{ph}$ is the level occupation number, which follows the Bose-Einstein distribution. Note that $\hbar\omega$ is the distance between the levels of the oscillator (see Fig. 2.1). The ratio between $P_d$ and $P_u$ represents the MP process rate and has the following expression [4]:

$$R_{MP} = \left(\frac{E_B}{\hbar\omega}\right)\left[P_d + exp\left(\frac{-\hbar\omega}{k_B T}\right)\left(\frac{P_u + \omega_e}{p_d + exp\left(\frac{-\hbar\omega}{k_B T}\right)}\right)\right], \tag{2.5}$$

where $E_B$ is the energy level of the last bonded state, $\omega_e$ is the inverse of the phonon life-time, and $k_B$ is the Boltzmann constant [4].

One of the most important advantages of the Hess model is that it takes into account the multiple combinations of MVE and AB processes. For example, a bond electron can be excited by multiple cold carriers to a medium level, and then a SP with enough energy (and with less energy than a SP excited from the ground state) can break the bond. With this consideration, the total bond-breakage rate is [4]:

$$R = \sum_{i=0}^{N_l}\left(\frac{I_{DS} f_v + \omega_e exp\left(\frac{-\hbar\omega}{k_B T}\right)}{I_{DS} f_v + \omega_e}\right)^i A^i I_{DS} f_d, \tag{2.6}$$

where $f_v$, $f_d$, and $A^i$ are empirical parameters used to introduce the macroscopical parameter $I_{DS}$.

This model has some shortcomings [4]:

- The life-time is computed as the time when $\Delta N_{it}$ achieves a threshold value, giving not correct estimations.
- The $\Delta N_{it}$ generation is not well connected to macroscopical quantities.

## 2.2 Rauch and La Rosa model (energy driven paradigm model)

Rauch and La Rosa changed the driven force paradigm of CHC degradation in short devices from the electric field to the carrier energy [4, 12, 33, 34, 35]. They showed that carrier energy plays an important role during CHC degradation. Following this paradigm, they suggested that the SP mechanism in short devices is due to the EES mechanism. In short channel devices, the probability of having a SP mechanism is close to zero, but according to this model, the EES mechanism changes this picture because it is able to provoke SP mechanisms [4, 33, 35]. In addition, the EES mechanism populates the tails of the carrier energy DF and enhances the CHC degradation when $T$ increases.

The AI used in this model has the following form:

$$AI \sim \int DF(E)S(E)dE, \tag{2.7}$$

where $DF(E)$ is the carrier energy DF and $S(E)$ is the cross section of the corresponding reaction. As $DF(E)$ decreases rapidly and $S(E)$ increases with a power law, the product of both functions shows two maxima (see Fig. 2.2), which can be related to empirical parameters such as stress voltages instead of carrier energies. In this way, the computational time decreases significantly.

The main shortcoming of this model is that it does not take into account the defect generation, which excludes the microscopic level of the CHC degradation.

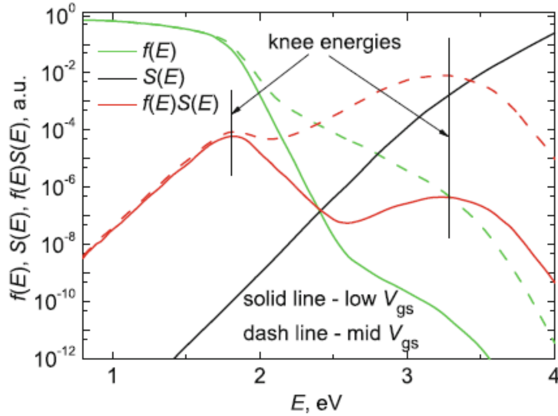


**Figure 2.2:** A sketch of the cross section function ($S(E)$), the carrier energy density function, ($DF(E)$, in the plot $f(E)$), and the product of both function ($DF(E)S(E)$). Figure taken from [4].

## 2.3 Bravaix model

The Bravaix model divides the CHC degradation mechanism in three independent modes. For the formulation, the Bravaix group uses the concept of lifetime instead of computing the carrier energy DF. These life-times are related to macroscopical parameters through empirical factors [5, 37]. This model intro-

duces the necessity of studying the carrier transport in order to correctly describe the physics of the three modes [5, 16, 36]. These modes are explained below.

1. The SP mechanism is activated when there are high average carrier energies. In this case the lifetime is [37, 38, 4]:

$$\frac{1}{\tau_{SP}} \sim \left(\frac{I_{DS}}{W}\right)\left(\frac{I_{BS}}{I_{DS}}\right)^{m}, \tag{2.8}$$

   where $W$ is the device width and $m \sim 2.7$ is an empirical factor.

2. The EES mechanism is activated when the flux and energy of the carriers are in an intermediate regime. The lifetime for this mode is [37, 38, 4]:

$$\frac{1}{\tau_{EES}} \sim \left(\frac{I_{DS}}{W}\right)^{2}\left(\frac{I_{BS}}{I_{DS}}\right)^{m}, \tag{2.9}$$

3. The MP process is activated when the channel carrier flux is high and the average of the carrier energy is low. In this mode, the Si-H bond is described as a truncated harmonic oscillator as in the Hess model [5, 36]. Here, the lifetime is:

$$\frac{1}{\tau_{MP}} \sim \left[ (qV_{DS} - \hbar\omega)^{1/2} \left( \frac{I_{BS}}{W} \right) \right]^{\frac{E_B}{\hbar\omega}} exp \left( \frac{-E_{emi}}{k_B T} \right)$$
$$\simeq \left[ V_{DS}^{1/2} \left( \frac{I_{BS}}{W} \right) \right]^{\frac{E_B}{\hbar\omega}} , \tag{2.10}$$

where $E_{emi}$ is the emission energy.

The device lifetime is the weighted combination of the three lifetimes as follows:

$$\frac{1}{\tau_d} = \frac{K_{SP}}{\tau_{SP}} + \frac{K_{EES}}{\tau_{EES}} + \frac{K_{MP}}{\tau_{MP}}, \tag{2.11}$$

where $\tau_d$ is the device lifetime and $K_{SP}$, $K_{EES}$, and $K_{MP}$ are parameters related to the probability of having a SP, EES or MP mechanisms. Following the Hess model, the Bravaix group arrives to the following system of differential equations [5]:

$$\frac{dn_0}{dt} = P_d n_1 - P_u n_o, \tag{2.12}$$

$$\frac{dn_i}{dt} = P_d(n_{i+1} - n_i) - P_u(n_i - n_{i-1}), \tag{2.13}$$

$$\frac{dn_N}{dt} = P_u n_{N-1} - P_d \Delta N_{it}[H^*], \tag{2.14}$$

where $[H^*]$ is the concentration of released hydrogen and $n_0$, $n_i$, and $n_N$ represent the occupation densities of the ground state, the $i$th level, and the last level, respectively. We can see that this model does not take into account combinations of MP and SP as the Hess model. The $P_u$ and $P_d$ rates are calculated with empirical parameters related to $I_{DS}$, reducing the computing time significantly. Another important advantage of this model is its ability to explain the temperature behaviour of the CHC degradation in short channel devices. In this case, the EES mechanism enhances the degradation process because it populates the tail of the carrier energy DF [5, 16].

Finally, the model has two important shortcomings [4]:

- The three modes are considered independent, which is not true because the carrier energy DF changes with respect to the stress time. In consequence, the weighted parameters must change. Therefore, a self-consistent model is necessary.
- In the newest version of the model [40], the authors say that the EES mechanism is overestimated but there is

some experimental evidence that shows the opposite [13].

## 2.4 Tyaginov and Bina model

The Tyaginov and Bina model solves the Boltzmann transport equation (BTE) in order to compute the carrier energy DF. In this way, the principal novelty of this model is the introduction of the transport perspective for the CHC degradation. The earlier version of the model uses the stochastic Boltzmann transport equation solver MONJU, which is based on Montecarlo methods [4, 13, 18]. The result of this simulation is the carrier energy DF for each discretized channel coordinate and for each stress time [4]. The DF is the input of the next module, which uses a simplified approach for solving the BTE. For this purpose, the MiniMOS simulator is used, which is based on the energy transport (ET) and drift-diffusion (DD) schemes [4]. The result of this step is the calculation of the principal characteristics of the degraded device. The AIs, used in the MONJU simulator, have the following form [4]:

$$AI^{(e/h)}_{SP/MP} = \int_{E_{TH}}^{\infty} f^{(e/h)}(E) g^{(e/h)}(E) \sigma^{(e/h)}_{SP/MP}(E) v(E) dE, \tag{2.15}$$

where $f^{(e/h)}(E)$ is the carrier DF for electrons/holes, $g^{(e/h)}(E)$ is the DOS, $v(E)$ is the group velocity, and $\sigma_{SP/MP}^{(e/h)}(E)$ is the Keldysh-like reaction cross section for the SP/MP mechanism. The model takes into account all possible combinations between AB (SP mechanism) and MVE (MP mechanism) processes, as the Hess model [4, 13, 18]. For instance, a cold carrier can excite the Si-H bond to an intermediate state and then, a SP can break the bond through an AB process. All these combinations are considered independent and weighted by probability coefficients [4, 13]. With all these considerations, there were two shortcoming with respect to this earlier version [4]:

- This model considers the combinations of SP and MP mechanisms independent. It is necessary a self-consistent point of view of these mechanisms.

- It is not possible to simulate short channel devices ($L < 100nm$) due to some restrictions in the MiniMOS simulator. The simplified vision of the ET and DD schemes precludes a good accuracy between experimental and simulated data.

The new model version uses the deterministic Boltzmann transport equation solver ViennaSHE. Previously, the device

structure is simulated by using Sentaurus Process, which is coupled with the ViennaSHE simulator [4, 13, 18]. This simulator takes into account some energy exchange mechanisms like: surface scattering, scattering at ionized impurities, impact ionization, electron-phonon scattering and EES [4, 13, 18]. Moreover, the model is able to simulate dipole moment interactions with the oxide electric field [4, 13]. As in the Hess model, all possible combinations between AB and MVE processes are considered, but in a self-consisted way. This means that these mechanisms compete to release the H atom in order to obtain a Si dangling bond [4, 13, 18]. In this model the AI for the AB process is:

$$AI_{AB}^{(e/h)} = \int_{E_{TH}}^{\infty} f^{(e/h)}(E) g^{(e/h)}(E) \sigma(E) v(E) dE, \qquad (2.16)$$

where

$$\sigma(E) = \begin{cases} \sigma_0 (E - E_{th})^{11} & \text{if } E \geq E_{TH} \\ 0 & \text{if } E < E_{TH}, \end{cases} \qquad (2.17)$$

where $\sigma_0$ is an attempt frequency. In the same way, the AI for the MVE process is:

$$AI_{AB}^{(e/h)} = \int_{E_{TH}}^{\infty} f^{(e/h)}(E) g^{(e/h)}(E) \sigma_0(E - \hbar\omega) v(E) dE, \quad (2.18)$$

Following the truncated harmonic oscillator model for representing the Si-H bond, a system of coupled differential equations (similar to equations (2.12), (2.13) and (2.14)) is obtained [4]. This system can be reduced to a single differential equation in order to compute $N_{it}$:

$$\frac{dN_{it}}{dt} = (N_0 - N_{it})\Re - N_{it}^2 \beta, \quad (2.19)$$

where $N_0$ is the number of initial interface states, $\Re$ is the cumulative bond breakage rate, and $\beta$ is the Arrhenius term for the thermal activation, which has the form:

$$\beta = \nu_p exp\left(\frac{-E_{pass}}{K_B T}\right), \quad (2.20)$$

where $\nu_p$ is the attempt rate and $E_{pass}$ is the pass energy (see Fig. 2.1). Eq. (2.19) shows that the CHC degradation increases the $\Delta N_{it}$ generation rate [4, 18].

This model is able to simulate, with very good accuracy with experimental data, the CHC degradation in long and short chan-

nel devices, as we can see in Ref. [4, 18]. As well, it is possible to analyse the contribution of each transport mechanism in the device degradation [13, 18]. Finally, the main shortcoming is related to the computing resources required for a single simulation [4].

# Chapter 3

# Experimental and Analytical Tools for Studying the Channel Hot Carrier Degradation under the Defect-Centric Point of View

The principal experimental and analytical tools, used in the present work, are studied in this chapter. First, we start with the principal CHC measurement techniques and then, we describe the defect-defect centric distribution.

## 3.1 Principal channel hot carrier measurement techniques

### 3.1.1 I-V stress

In this technique, the initial $V_{TH0}$ is measured from a complete $I_{DS} - V_{GS}$ characteristic with a $V_{DS} = 50mV$. Then, the gate and drain terminals are stressed. This stress condition is interrupted several times in order to measure complete $I_{DS} - V_{GS}$ curves in order to extract a new $V_{TH}$ (after stress) [41]. The $V_{TH}$ shift is extracted as follows:

$$\Delta V_{TH} = V_{TH0} - V_{TH}. \tag{3.1}$$

We can see some typical $I_{DS} - V_{GS}$ characteristics for several stress times in Fig. 3.1. At the end, we obtain one $\Delta V_{TH}$ for each stress time. The principal shortcoming of this technique is that the recoverable degradation component is not well measured due to the time needed for taking a complete $I_{DS} - V_{GS}$ curve [41]. This effect is stronger in BTI measurements while is weak in CHC experiments due to the permanent nature of the degradation (the generated interface traps are permanent).

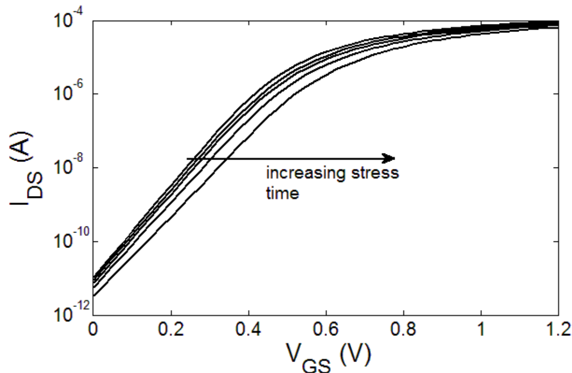


**Figure 3.1:** $I_{DS} - V_{GS}$ characteristics for several stress times. We can see that the characteristic curve moves to the right when the stress time increases, showing an increment of $V_{TH}$. In the I-V stress technique, the $V_{TH}$ is extracted from the complete curve.

### 3.1.2 Measure-Stress-Measure (MSM) technique

Firstly, a complete $I_{DS}-V_{GS}$ characteristic is measured without any stress. Then, a logarithmic stress pulse is applied to the drain and gate terminals as we can see in Fig. 3.2 [41]. The part of the pulse related to the stress increases logarithmically while the time where the measurement is done (sense) is constant with $t_{sense} = 0.5s$ in our experiments. During the stress time, the

drain and gate terminals are set to $V_{Gstress}$ and $V_{Dstress}$ (these values depend on the experiment). During the sense time, we apply $V_{Gsense} = 0.5V$ (close to $V_{TH}$) and $V_{Dsense} = 0.05V$ and we measure $I_{DS}$. These $I_{DS}$ measurements are transformed into $\Delta V_{TH}$ values by projecting them into the initial $I_{DS} - V_{GS}$ curve (measured before applying the stress pulse) as we show in Fig. 3.3. This technique enables us to measure the recoverable component of the degradation [41].

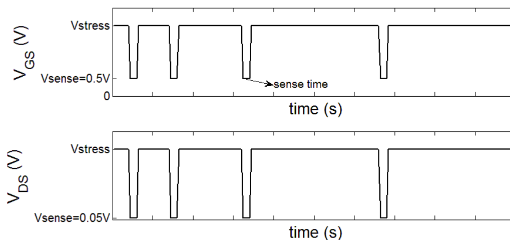


**Figure 3.2:** An example of a logarithmic stress pulse of the MSM technique. Top: the stress pulse for the gate terminal. Bottom: the stress pulse for the drain terminal. In this case, $V_{Gsense} = 0.5V$ and $V_{Dsense} = 0.05V$.

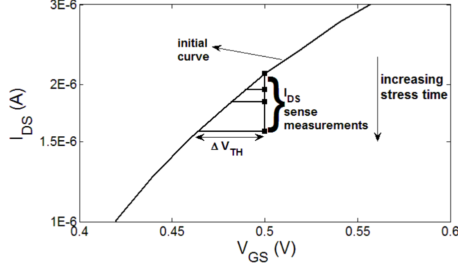


**Figure 3.3:** In the MSM technique, during the sense time, the $I_{DS}$ current is measured several times according to the logarithmic pulse (square dots). These values are projected into the initial $I_{DS} - V_{GS}$ curve in order to extract the $\Delta V_{TH}$ value.

## 3.2 The defect-centric distribution

It is well known that the $V_{TH}$ shift generated by a single charge follows an exponential distribution with mean value $\eta$ [42, 43, 44]. The principal expressions for this distribution are: [20, 44]:

$$f_{\eta}(\Delta V_{TH}) = \frac{1}{\eta} exp\left(\frac{\Delta V_{TH}}{\eta}\right), \tag{3.2}$$

$$F_{\eta}(\Delta V_{TH}) = 1 - exp\left(\frac{\Delta V_{TH}}{\eta}\right), \tag{3.3}$$

where $f_\eta$ and $F_\eta$ are the probability density function and the cumulative function, respectively. If we consider $n$ of these single defects in a device (*device level*), we have that the total $\Delta V_{TH}$ is equal to the convolution of the $n$ individual exponential distributions [20, 44]. In this case, we have:

$$g_{\eta,n}(\Delta V_{TH}) = \frac{\Delta V_{TH}^{(n-1)}}{\eta^n (n-1)!} exp\left(\frac{\Delta V_{TH}}{\eta}\right), \tag{3.4}$$

$$G_{\eta,n}(\Delta V_{TH}) = 1 - \frac{1}{(n-1)!}\Gamma(n, \Delta V_{TH}/\eta), \tag{3.5}$$

where $g_{\eta,n}$ is the probability density function, $G_{\eta,n}$ is the cumulative function and $\Gamma$ is the Gamma function. The total number of traps, in several devices (*chip level*), are Poisson distributed with mean value $N_t$ [45, 46, 47]. In this case, the probability density function is:

$$P_{N_t}(n) = \frac{exp(-N_t)N_t^n}{n!}. \tag{3.6}$$

Hence, the total $\Delta V_{TH}$ in a chip is the sum of $G_{\eta,n}$ weighted by $P_{N_T}(n)$ [20, 44]:

$$H_{\eta,N_t}(\Delta V_{TH}) = \sum_{n=0}^{\infty} \frac{e^{-N_t} N_t^n}{n!} G_{\eta,n}(\Delta V_{TH}) \tag{3.7}$$

or

$$H_{\eta,N_t}(\Delta V_{TH}) = \sum_{n=0}^{\infty} \frac{e^{-N_t} N_t^n}{n!} \left[1 - \frac{\Gamma\left(n, \Delta V_{TH}/\eta\right)}{(n-1)!}\right], \quad (3.8)$$

where $H_{\eta,N_t}$ is the cumulative function of the defect-centric distribution. The advantage of using the DCD is that its first and second moments are related to physical parameters as follows [19, 20, 21, 53]:

$$\langle \Delta V_{TH} \rangle = N_t \eta, \quad (3.9)$$

$$\sigma^2 = 2 N_t \eta^2. \quad (3.10)$$

where $\langle \Delta V_{TH} \rangle$ is the expected value of $\Delta V_{TH}$ and $\sigma^2$ is the distribution variance. Finally, for computing the cumulative distribution of the experimental $\Delta V_{TH}$ data, it is necessary to sort them and then, apply a ranking algorithm. In our case, we have used the Benard approximation [48]:

$$H(i) = \frac{i - 0.3}{n + 0.4}. \quad (3.11)$$

where $i$ is the position of a sorted experiment and $n$ is the total number of experiments.

# Chapter 4

# Study of the Geometry Device Dependence of the Defect-Centric Parameters

In this chapter, we study the dependence of principal defect-centric parameters with respect to the device geometry. We show that the DCD explains very well the CHC degradation behaviour. As well, we demonstrate that the CHC degradation strongly depends on the channel length and weakly depends on the device width.

## 4.1 Defect-centric distribution of experimental data of CHC-induced $\Delta V_{TH}$

Fig. 4.1 shows the experimental data and their fittings with the DCD of 50 CHC degradation experiments for several stress times. The MSM technique was used over bulk planar nMOSFETS with an effective channel length ($L_{eff}$) of $100nm$, $W = 85nm$ and a gate dielectric of $1.8nm$ of SiON [49]. The stress conditions were: $V_{Gstress} = V_{Dstress} = 2.0V$, which represents the most degrading CHC stress condition for short channel devices. The sense voltages were: $V_{Gsense} = 0.5V$ and $V_{Dstress} = 50mV$ (see Fig. 3.2) [49]. In the $x - axis$, we have the CHC-induced threshold voltage shift values for several times, and in the $y - axis$, we have the cumulative distribution, $H(i)$, in probit scale. For computing $H(i)$, we have used the Bernard ranking algorithm (see eq. 3.11). In these experiments, we can see that the DCD fits very well from $-2\sigma$ to $2\sigma$.

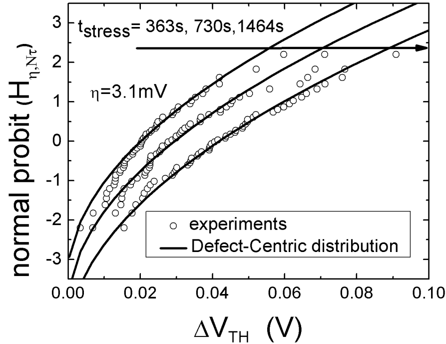


**Figure 4.1:** Distributions of the CHC-induced $\Delta V_{TH}$ for several stress times. We can see that $\eta$ is constant and the variation of $< \Delta V_{TH} >$ is only due to the increment of $N_t$. In this case: $V_{Gstress} = V_{Dstress} = 2V$.

In Fig. 4.1, we can see that the defect-centric parameter $\eta$ (related to the second moment) is constant with respect to the stress time and the increment of t$< \Delta V_{TH} >$ is directly related to the increase of $N_t$, according to eq. (3.9). This can be seen in Fig. 4.2, where $N_t$ and $t_{stress}$ follow a power law with exponent 0.45, which agrees well with the typical values for CHC degradation (0.4 $\sim$ 0.6) [5, 6, 11]. In addition, this value shows that the principal degradation mechanism is the generation of interface traps according to Ref. [11]. Note that

the DCD takes into account the traps formed at the interface and those generated in the oxide [21, 49].

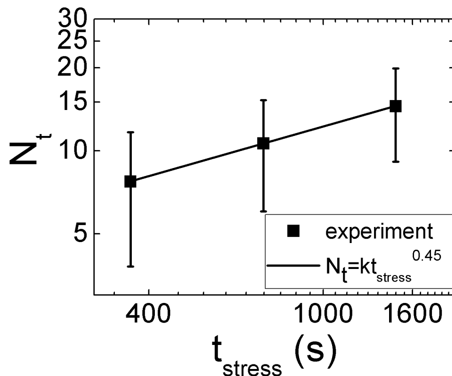


**Figure 4.2:** $N_t$ increases with respect to $t_{stress}$. The exponent of the power law $N_t = t^n$ is 0.45.

Figures 4.3 and 4.4 show more fittings of CHC degradation experiments with the DCD for several stress times. In these cases, the tests were done on nMOSFETs processed in 45$nm$ and 65$nm$ bulk planar CMOS commercial technologies [50]. We have performed 160 experiments per technology. The channel width is 1$\mu m$ for both processes and the effective channel lengths are 37$nm$ and 50$nm$ for the 45$nm$ and 65$nm$ technologies, re-

spectively. The gate dielectric consists of $1.85nm$ of SiON. In this case, we use the $I - V$ technique for the CHC degradation measurements. The stress conditions are: $V_{Gstress} = 1.1V$ and $V_{Dstress} = 1.8V$ for the $45nm$ technology, and $V_{Gstress} = 1.2V$ and $V_{Dstress} = 1.8V$ for the $65nm$ technology [50]. We can see that the DCD fits very well with the experimental data up to $3\sigma$ [50].

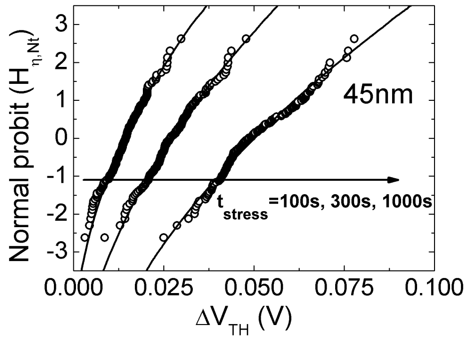


**Figure 4.3:** CHC-induced $\Delta V_{TH}$ follows a DCD in $45nm$ commercial technology. In this case: $V_{Gstress} = 1.1V$ and $V_{Dstress} = 1.8V$.

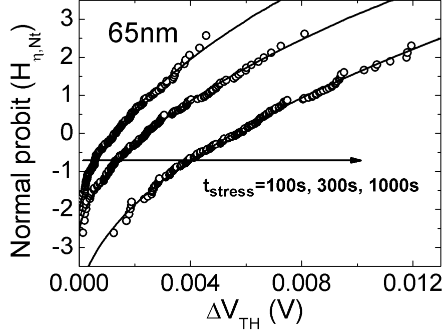


**Figure 4.4:** CHC-induced $\Delta V_{TH}$ follows a DCD in $65nm$ commercial technology. In this case: $V_{Gstress} = 1.2V$ and $V_{Dstress} = 1.8V$.

## 4.2 Length and width dependences of the defect-centric parameters

For studying the channel length dependence of the defect-centric parameters, we take into account the effective length ($L_{eff}$, which represents only the channel length of a device), instead of the total length ($L$, which takes into account the channel length and the overlaps). We have extracted the defect-centric parameters for three different $L_{eff}$: $120nm$, $70nm$ and $40nm$. For

these cases, the device width is 90$nm$ (constant). For the width dependence, we have chosen four different $W$: 70$nm$, 85$nm$, 100$nm$ and 200$nm$ with a constant $L_{eff}$ = 100$nm$. For both groups of experiments, the gate stack consists of 1.8$nm$ of SiON. We have used the MSM stress technique with the same stress conditions for both groups: $V_{Gstress} = V_{Dstress} = 2V$. The sense voltages were: $V_{Gsense} = 0.5V$ and $V_{Dsense} = 50mV$ with a $t_{sense} = 0.5s$. The defect centric parameters: $\eta$ and $N_t$ were extracted from the first and second moment of the DCD by applying eq. (3.9) and .eq. (3.10).

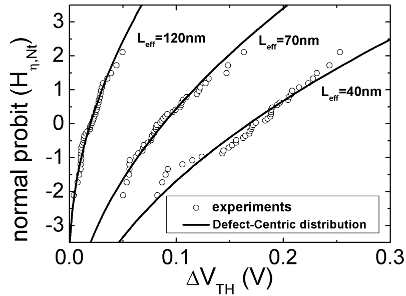


**Figure 4.5:** $\Delta V_{TH}$ for different $L_{eff}$ and same $W = 90nm$. The first and second moments strongly decrease with $L_{eff}$.

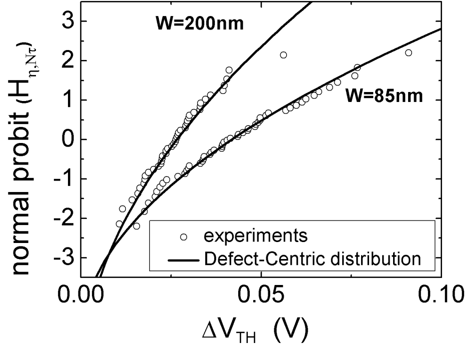


**Figure 4.6:** $\Delta V_{TH}$ for different $W$ and same $L_{eff} = 100nm$. The first and second moments weakly decrease with $W$.

Figures 4.5 and 4.6 show the $\Delta V_{TH}$ distributions for different $L_{eff}$ and $W$. We can see that the DCD has stronger dependence on $L_{eff}$ than $W$. In both cases, $\eta$ ( second moment of the DCD) decreases with $L_{eff}$ and $W$, whereas the first moment ($< \Delta V_{TH} >$) strongly increases with $L_{eff}$ and weakly increases with $W$; this can also be seen in Fig. 4.7. These tendencies are better explained in Fig. 4.8, where $\eta$ is plotted in function of the effective area ($A_{eff}$), and in Fig. 4.9, where the number of traps is shown in function of the studied dimension. Fig. 4.8 shows that $\eta$ is inversely proportional to $A_{eff}$ and, there-

fore, to $L_{eff}$ and $W$. The same result has been reported for BTI degradation in [21, 51]. Fig. 4.9 shows that $N_t$ decreases with $L_{eff}$ and increases with $W$. In one hand, we have that $< \Delta V_{TH} >$ and $\sigma$ strongly decrease with the increment of $L_{eff}$ due to the diminution of $\eta$ and $N_t$. On the other hand, we have that $< \Delta V_{TH} >$ and $\sigma$ weakly decrease with the increment of $W$ because the diminution of $\eta$ is partiality compensated by the increment of $W$.

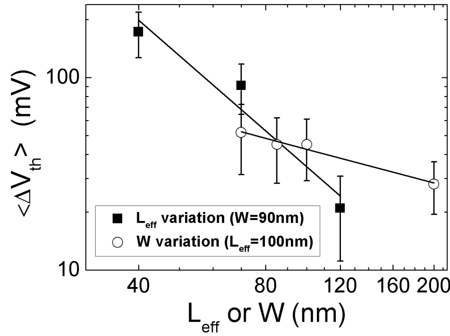


**Figure 4.7:** $< \Delta V_{TH} >$ as function of $L_{eff}$ or $W$. The expected value of $\Delta V_{TH}$ strongly decreases with $L_{eff}$ and weakly decreases with $W$.

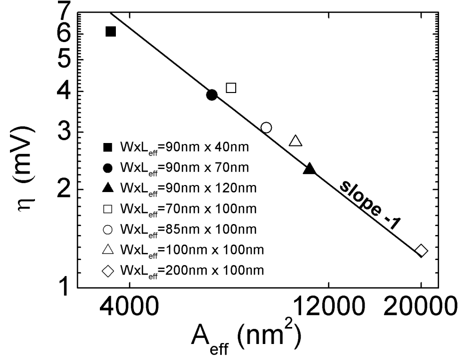


**Figure 4.8:** $\eta$ scales as $1/A_{eff}$.

In Fig. 4.10, we plot the density of traps, $D_t = N_t/A_{eff}$, in function of $L_{eff}$ or $W$. We can see that $D_t$ strongly decreases with $L_{eff}$ due to the higher lateral electrical field applied during the CHC degradation. The weak increment of $D_t$ with respect to $W$ can be attributed to some process related non-uniformities of the gate dielectrics along the shallow trench isolation edge [52] and it explains the soft decrement of $< \Delta V_{TH} >$ when $W$ increases. In BTI degradation, it has been reported that $D_t$ is constant [21, 53]; therefore, the BTI-induced $\Delta V_{TH}$ does not change with respect to $L_{eff}$ and $W$. Thus, this strong change

of $< \Delta V_{TH} >$ with respect to $L_{eff}$ is the *signature of the CHC mechanism.*

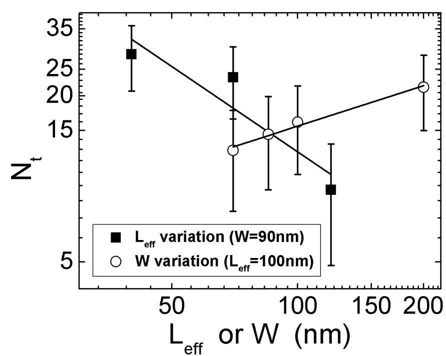


**Figure 4.9:** $N_t$ as function of $L_{eff}$ or $W$. $N_t$ decreases with $L_{eff}$ and increases with $W$.

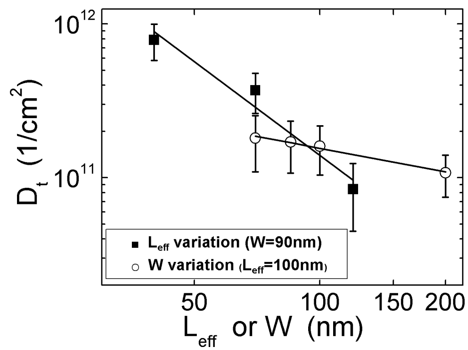


**Figure 4.10:** $D_t$ as function of $L_{eff}$ or $W$. $D_t$ strongly decreases with $L_{eff}$ and slightly decreases with $W$.

# Chapter 5

# A Defect-Centric Analysis of the Temperature Dependence of the Channel Hot Carrier Degradation

In this chapter, we study the temperature dependence of the defect-centric parameters, $\eta$ and $N_t$. The experiments were carried out in bulk planar nMOSFETs with $W = 90nm$ and $L_{eff} = 40nm$. The gate stack consists of $1.8nm$ of SiON. The temperature range varies from $25°C$ to $150°C$ in steps of $25°C$. We performed 30 experiments per temperature, giving a total population of 180 devices. For generating the CHC stress, we have used the MSM technique with the following conditions:

$V_{Dstress} = V_{Gstress} = 1.6V$ (maximum damage condition) and $V_{Dsense} = 50mV$ and $V_{Gsense} = 0.5V$. In order to compare results, we perform CHC stress measurements in wider devices ($W = 1\mu m$, $L_{eff} = 40nm$) with the same stress conditions.

## 5.1 Temperature dependence of the defect-centric parameters

Fig. 5.1 shows the $\Delta V_{TH}$ distribution for several temperatures. We can see that experimental data fits well with the DCD. According to Fig. 5.1 and Fig. 5.2, $< \Delta V_{TH} >$ increases with $T$ in agreement with previous CHC experiments [5, 6, 7, 16]. This tendency can be explained by the activation of the EES mechanism which is dominant at high energies in the carrier energy DF, according to Bravaix model [5, 16]. In order to understand the physics of microscopic mechanisms for explaining these macroscopic results, we have extracted the defect centric parameters in function of the studied temperature range.

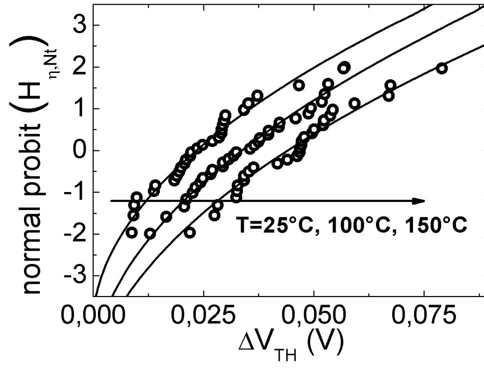


**Figure 5.1:** CHC-induced $\Delta V_{TH}$ distribution for several temperatures. All experiments agree well with the DCD. We can see that $< \Delta V_{TH} >$ increases with $T$.

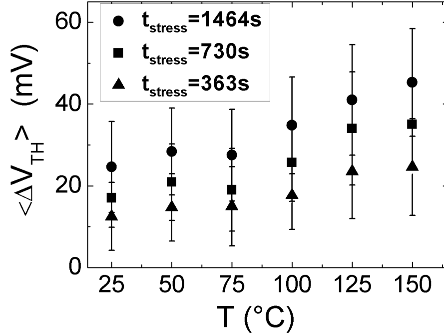


**Figure 5.2:** The expected value of the CHC induced $V_{TH}$ shift increases with $T$ in agreement to the activation of the EES mechanism.

On one hand, Fig. 5.3 shows that the total number of traps, $N_t$, and the density of traps $D_t$ increase with $T$. On the other hand, Fig. 5.4 shows that $\eta$ is independent of the temperature. It is important to mention that the temperature independence of $\eta$ has also been reported for BTI degradation [54]. These two results show that the increment of the CHC degradation with respect to $T$ (measured on the increase of $< \Delta V_{TH} >$) is ascribed to the higher number of generated defects and not to the higher impact of defects on $V_{TH}$. This physical interpretation agrees well with the enhancement of the defect generation due

to the activation of the EES mechanism [16, 18].

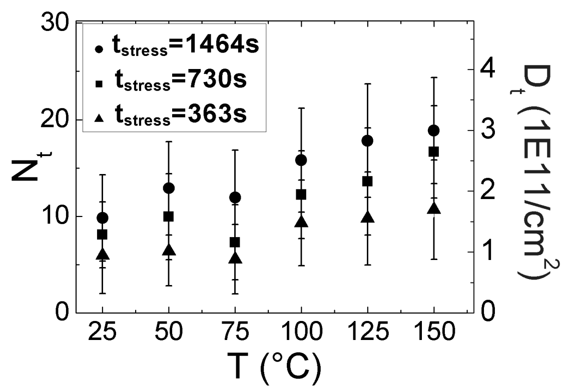


**Figure 5.3:** $N_t$ increases as function of $T$. On the right axis, $D_t$ is plotted.

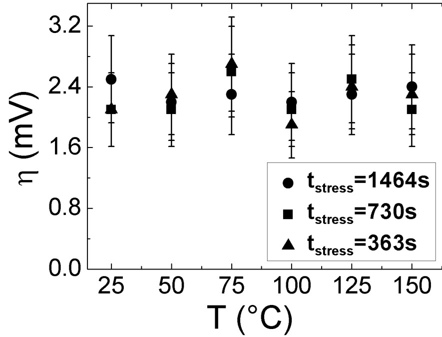


**Figure 5.4:** $\eta$ is independent of $T$.

During the the CHC stress, the oxide close to the drain terminal is affected by CHC degradation mechanisms, whereas the oxide close to the source terminal experiences the cold carrier injection due to the high oxide electric field, resulting in a positive bias temperature instability (PBTI) degradation. In order to study the contribution of the PBTI component in the total device degradation, we have performed PBTI measurements in the short devices with the same stress condition on the gate terminal. We have obtained a $\Delta V_{TH} \simeq 1.25mV$ for a $t_{stress} = 1464s$ at $T = 125°C$; therefore, the PBTI contribution can be neglected in comparison with the CHC component.

Thus, the observed temperature dependence is only ascribed to CHC degradation.

## 5.2 Extraction of the activation energy

Fig. 5.5 shows the Arrhenius plot of $N_t$ for several stress times. We have extracted an average value of $\simeq 58meV$ for the $E_{ACT}$, which is similar to that obtained in BTI degradation ($E_{ACT} \simeq 60meV$) [54]. The extracted $E_{ACT}$ is related to the following empirical expression [54]:

$$N_t \propto exp\left(\frac{-E_{ACT}}{k_B T}\right)\left(\frac{V_{GS} - V_{TH0}}{t_{ox}}\right) t_{stress}^{n}, \quad (5.1)$$

where $t_{ox}$ is the oxide thickness, and $V_{TH0}$ is the initial threshold voltage measured before applying the stress. According to the DCD and our experimental results, we have that: $< V_{TH} >= \eta N_t$ and $\eta$ is constant; therefore, $< V_{TH} >$ also follows an empirical rule like eq. (5.1). In Fig. 5.6, we show the Arrhenius plot of $< \Delta V_{TH} >$ for small devices ($90nm$ x $40nm$) and wider devices ($1\mu m$ x $40nm$). The activation energies ($E_{ACT}$) are very similar for both geometries and close to the value calculated for $N_t$ (small devices: $E_{ACT} \simeq 53meV$ and

wider devices: $E_{ACT} \simeq 56meV$).
Finally, in order to calculate the activation energy related to the failure time, in Appendix A, we have shown that both activation energies are related by:

$$< E_{A_{capture}} >= \frac{1}{n} E_{ACT}, \qquad (5.2)$$

where $< E_{A_{capture}} >$ is the activation energy related to the failure time, and $n$ is the exponent of the power law: $N_t = Kt^n$ (which is in the range $0.4 \sim 0.6$ for CHC degradation). In our experiments, we have found that $< E_{A_{capture}} >= 0.117eV$, where an extracted $n = 0.45$ was used.

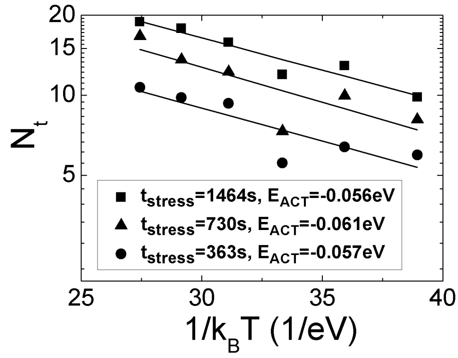


**Figure 5.5:** Arrhenius plot of $< \Delta V_{TH} >$ for small and large devices. For both geometries, similar values of $E_{ACT}$ are obtained.

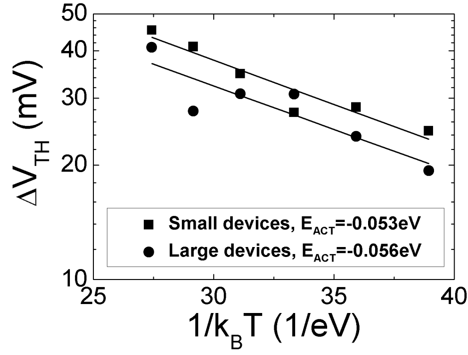


**Figure 5.6:** Arrhenius plot of $N_t$ for several stress times. $E_{ACT}$ values are similar to those obtained for BTI degradation.

# Chapter 6

# A Defect-Centric Study of the Channel Hot Carrier Variability

In this chapter, we begin studying the principal variability concepts. Then, we perform an analysis, based on the DCD, in order to study the dependence of $< \Delta V_{TH} >$ with respect to the drain voltage and stress time. Finally, the time-zero variability and the time-dependent variability of the CHC degradation are studied.

## 6.1 Variability concepts

The mismatch of a parameter $X$ measured in a pair of matching devices is defined by [9]:

$$\delta X = X_A - X_B, \tag{6.1}$$

where $\delta X$ is the mismatch of the parameter $X$, and $X_A$ and $X_B$ are measurements of the $X$ parameter on devices $A$ and $B$, respectively. In this chapter, we study the mismatch of:

i) the initial threshold voltage measured before applying the stress or *time-zero mismatch*: $\delta V_{TH0} = V_{TH0_A} - V_{TH0_B}$, and

ii) the threshold voltage shift measured after applying the CHC stress or *time-dependent mismatch*: $\delta \Delta V_{TH} = \Delta V_{TH_A} - \Delta V_{TH_B}$.

We use the following nomenclature: $\delta$ denotes the difference between paired devices and $\Delta$ denotes a CHC-induced shift in one device. The total mismatch of $V_{TH}$ after stress is the sum of the time-zero mismatch and the time-dependent mismatch [9]:

$$\delta V_{TH} = \delta V_{TH0} + \delta \Delta V_{TH}. \tag{6.2}$$

Thus, there are two sources of fluctuations for computing $\delta V_{TH}$: fluctuations related to $V_{TH0}$ (pristine devices or time-zero) and fluctuations due to CHC (time-dependent) [9]. The variance of $\delta V_{TH}$ can be computed by [9]:

$$\sigma^2_{\delta V_{TH}} = \sigma^2_{\delta V_{TH0}} + \sigma^2_{\delta \Delta V_{TH}} + 2\rho\sigma_{\delta V_{TH0}}\sigma_{\delta \Delta V_{TH}}, \tag{6.3}$$

where $\sigma^2_{\delta V_{TH}}$ is the variance of the total $V_{TH}$ mismatch, $\sigma^2_{\delta V_{TH0}}$ is the variance of the time-zero mismatch, $\sigma^2_{\delta \Delta V_{TH}}$ is the variance of the time-dependent mismatch and $\rho$ is the correlation factor between time-zero fluctuations and time-dependent fluctuations. Note that the variability is defined as the standard deviation of the mismatch [9].

In addition, there are two kind of sources of variability: systematic (or extrinsic) and random (or intrinsic) [55, 56]. Systematic sources are process related and affect the real values of the extracted parameters. In this perspective, the time-zero variability has been well-studied in deeply-scaled very-large-scale integration (VLSI) technologies. For example, in Ref. [57] the time-zero threshold voltage ($V_{TH0}$) distribution has been studied up to 5.4$\sigma$ on 11 billions of transistors. As result, this distribution

is assumed to be normal with mean value $< V_{TH0} >$ and variance $\sigma_{V_{TH0}}$ [57]. The random component of $\sigma_{V_{TH0}}$ scales with respect to the area, as follows [58, 59, 60]:

$$\sigma^2_{V_{TH0},int} = \frac{K^2_{V_{TH0}}}{A}, \tag{6.4}$$

where $K_{V_{TH0}}$ is a scaling parameter, $A$ is the device area, and the sub-index *int* represents the intrinsic (random) component. The time-dependent variability has also been studied under the defect-centric framework in Ref. [55, 56], where the use of matching pair devices (MPD) enables to extract the random component of the time-dependent variability as follows (see Appendix B for the demonstration) [50, 55, 56]:

$$\sigma^2_{\Delta V_{TH},int} = \frac{\sigma^2_{\delta \Delta V_{TH}}}{2}. \tag{6.5}$$

The same approach can be applied to the time-zero variability [55, 56]:

$$\sigma^2_{V_{TH0},int} = \frac{\sigma^2_{\delta V_{TH0}}}{2}, \tag{6.6}$$

Thus, the total variance of the CHC-induced $\Delta V_{TH}$ is:

$$\sigma^2_{\Delta V_{TH}} = \sigma^2_{\Delta V_{TH},int} + \sigma^2_{\Delta V_{TH},ext}, \tag{6.7}$$

where the sub-index *ext* is used for representing the extrinsic variability component. In the defect-centric framework, we have that $\eta^2$ is directly proportional to the variance of the CHC-induced $\Delta V_{TH}$ distribution: $\sigma^2_{\Delta V_{TH}} = 2N_t\eta^2$. Therefore, the total $\eta$ also has two components:

$$\eta = \eta_{int} + \eta_{ext}, \tag{6.8}$$

where $\eta_{int}$ is considered the *correct* value. In this context, for studying the time-dependent variability, we use the defect-centric parameter, $\eta$, instead of $\sigma_{\Delta V_{TH}}$.

## 6.2 Experimental results

The experiments were carried on two groups of nMOSFETs processed in $45nm$ and $65nm$ bulk planar commercial technologies. For both technologies, the width is $1\mu m$ and the effective channel lengths are estimated to be $37nm$ and $50nm$ for the technologies of $45nm$ and $65nm$, respectively. The gate stack consists of $1.85nm$ of SiON. The $I - V$ technique was used for generating the CHC stress with the following conditions:

- $45nm$ technology: $V_{Dstress} = 1.7V$, $1.8V$ and $1.9V$, $V_{Gstress} = 1.1V$

- $65nm$ technology: $V_{Dstress} = 1.8V$, $2.0V$, $2.2V$ and $2.4V$, $V_{Gstress} = 1.2V$

The measurements were done over 80 MPD for each stress configuration, giving an overall population of more than 1000 samples.

### 6.2.1 Drain voltage and stress time dependences

As we mentioned in previous sections, $N_t$ follows a power law with respect to $t_{stress}$ with an exponent in the range $0.4 \sim 0.6$. If we consider that $\eta$ is constant with respect to $t_{stress}$ (as we show in section 4.1), and by using the defect-centric expression: $< \Delta V_{TH} >= N_t \eta$, we have that $< \Delta V_{TH} >$ should also follow a power law with respect to $t_{stress}$ with an exponent in the same range as $N_t$. This tendency can be seen in Figs. 6.1 and 6.2. In these plots, the average slope is $\sim 0.55$ [50]. Moreover, we have also found the same tendency for the $V_{Dstress}$ dependence, where $< \Delta V_{TH} >$ follows a power law with respect to $V_{Dstress}$ with a slope of $\sim 12.5$, as we can see in Figs. 6.3 and 6.4 [50].

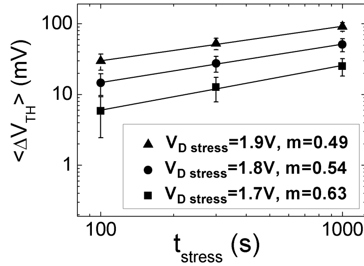


**Figure 6.1:** The expected value of the CHC-induced $\Delta V_{TH}$ follows a power law with respect to $t_{stress}$ with an average slope of $\sim 0.55$ for the $45nm$ technology.

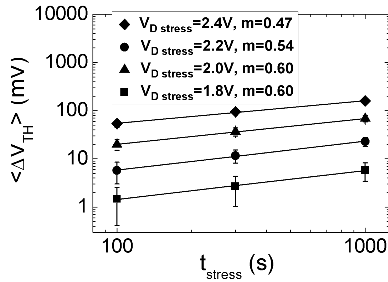


**Figure 6.2:** The expected value of the CHC-induced $\Delta V_{TH}$ follows a power law with respect to $t_{stress}$ with an average slope of $\sim 0.55$ for the $65nm$ technology.

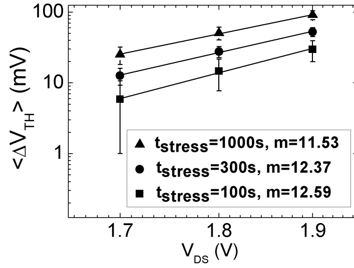


**Figure 6.3:** The expected value of the CHC-induced $\Delta V_{TH}$ follows a power law with respect to $V_{Dstress}$ with an average slope of $\sim 0.12$ for the $45nm$ technology.

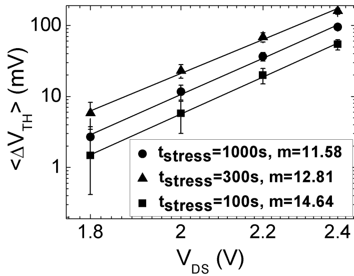


**Figure 6.4:** The expected value of the CHC-induced $\Delta V_{TH}$ follows a power law with respect to $V_{Dstress}$ with an average slope of $\sim 0.13$ for the $65nm$ technology.

### 6.2.2 Time-zero variability

Fig. 6.5 shows the distribution of $V_{TH0}$ in a normal probit scale (NP) for both technologies. We can see that $V_{TH0}$ follows a normal distribution up to $3\sigma$ in pristine devices in agreement with Ref. [57]. Fig. 6.6 shows the distribution of the mismatch of $V_{TH0}$ for both technologies. We can see that the variability of the $45nm$ technology is higher than the $65nm$ technology, in agreement with the scaling rule $1/A_{eff}$ (see equation (6.4)) [56]. As well, the $\delta V_{TH0}$ data follows a normal distribution up to $3\sigma$. Fig. 6.7 shows the total and the intrinsic time-zero variabilities. We have extracted the intrinsic variability by applying equation (6.6). As we expected, the intrinsic (random) variability is lower than the total one.

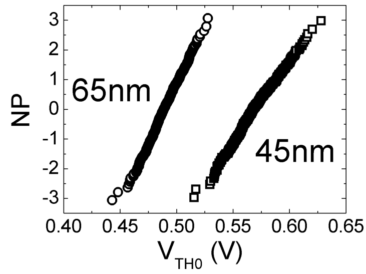


**Figure 6.5:** The time-zero $V_{TH0}$ follows a normal distribution up to $3\sigma$ for both technologies.

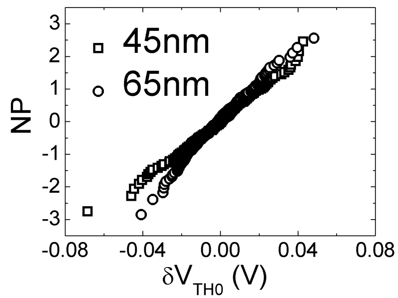


**Figure 6.6:** The time-zero mismatch follows a normal distribution up to $3\sigma$ for both technologies.

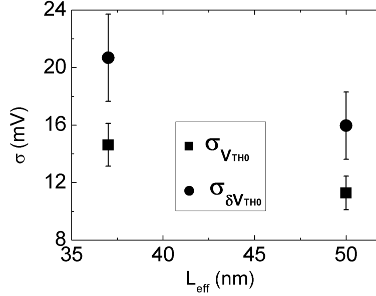


**Figure 6.7:** Total and intrinsic time-zero variabilities in function of the effective channel length for both technologies.

### 6.2.3 Time-dependent variability

Figs. 6.8 and 6.9 show the $\Delta V_{TH}$ mismatch for both technologies. We can see that the variability increases with $t_{stress}$ due to the increment of $< \Delta V_{TH} >$ (see Fig. 6.1 and Fig. 6.2). In addition, these mismatch data follow a normal distribution up to $3\sigma$.

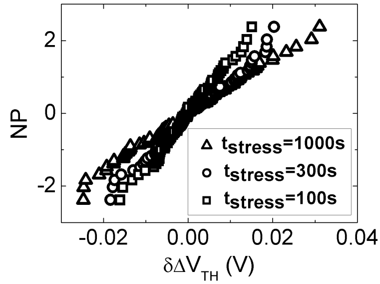


**Figure 6.8:** The time-dependent mismatch follows a normal distribution up to $3\sigma$ for several stress times in $45nm$ technology.

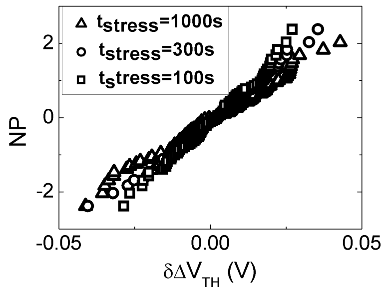


**Figure 6.9:** The time-dependent mismatch follows a normal distribution up to $3\sigma$ for several stress times in $65nm$ technology.

In Figs. 6.10 and 6.11 we can see that $\eta$ is practically independent of the stress time in single devices (total $\eta$) and in MPD (intrinsic or correct $\eta$); whereas in Figs. 6.12 and 6.13, we can see the independence of $\eta$ (total and intrinsic) with respect to $V_{Dstress}$. Here, we have used equation (6.5) for extracting the intrinsic values of $\eta$. As we expected, a lower time-dependent variability is obtained in MPD in function of $t_{stress}$ and $V_{Dstress}$.

We can observe that the $45nm$ technology exhibits a higher time-dependent variability than the $65nm$ technology. This is ascribed to the scaling rule $\eta \propto 1/A_{eff}$ reported in section 4.2. In BTI degradation $\eta$ is in the range: $\eta_0 \leq \eta \leq 2\eta_0$ with:

$$\eta_0 = \frac{q}{C_{ox}}, \tag{6.9}$$

where $q$ is the elementary charge and $C_{ox}$ is the oxide capacitance. We can see in figures 6.10, 6.11, 6.12 and 6.13 that the extracted values of $\eta$ are higher than the BTI range. This occurs because of the *non uniform* degradation region formed during CHC stress [50, 55]. Thus, the value of $\eta$ can increase or decrease with respect to stress parameters, depending on the *lateral extend* and the *magnitude* of the degraded region [50, 55].

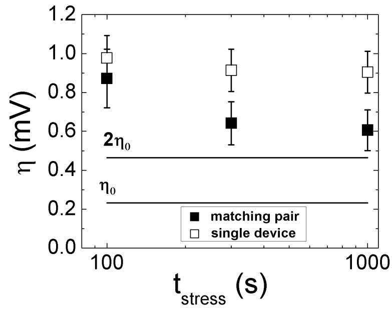


**Figure 6.10:** The time-dependent variability is practically independent of the stress time in 45$nm$ technology.

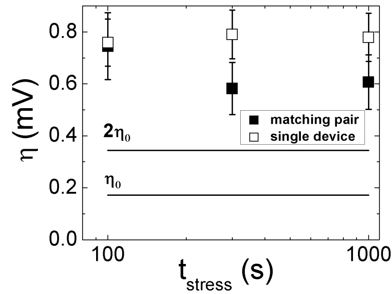


**Figure 6.11:** The time-dependent variability is practically independent of the stress time in 65$nm$ technology.

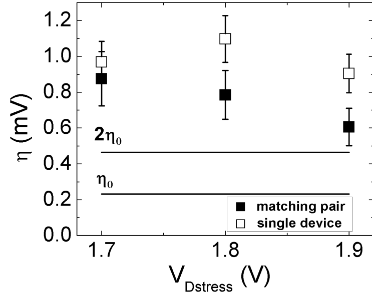


**Figure 6.12:** The time-dependent variability is practically independent of the drain voltage in 45$nm$ technology.

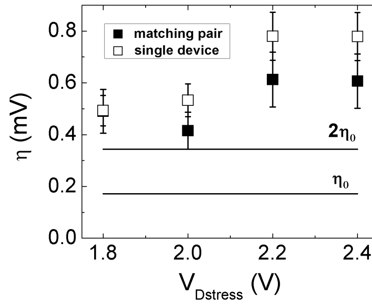


**Figure 6.13:** The time-dependent variability is practically independent of the drain voltage in 65$nm$ technology.

# Chapter 7

# General Conclusions and Future Work

## 7.1 Conclusions

The CHC degradation under the defect-centric point of view has been studied. Particularly, we have analysed the behaviour of the defect-centric parameters: $\eta$, $N_t$ and $< V_{TH} >$ under the variation of different parameters: $L_{eff}$, $W$, $t_{stress}$, $V_{Dstress}$ and $T$. In addition, we have studied the variability of the defect-centric parameters by using MPD. For generating the CHC stress, we have used the $I - V$ and MSM techniques. In to-

tal we have performed more than 1400 experiments.

We have demonstrated that the DCD is able to describe well the experimental data of the CHC degradation up-to $3\sigma$. We have showed that $< V_{TH} >$ and $N_t$ follow a power law with respect to $t_{stress}$ with an exponent in the range of $0.45 \sim 0.55$, which coincide with typical values for CHC degradation. One of the most important results we have found, is the following scaling rule: $\eta \propto 1/A_{eff}$, which coincides with BTI degradation. As well, $< V_{TH} >$ strongly increases with the diminution of $L_{eff}$ and weakly increases with the diminution of $W$. In addition, $N_t$ decreases with $L_{eff}$ and increases with $W$; whereas $D_t$ (normalized $N_t$) strongly decreases with $L_{eff}$ and weakly decreases with $W$. Below, we can find the explanations for these tendencies:

- For the $W$ dependence: when $W$ increases, the decrement of $\eta$ is partially compensated by the increment of $N_t$, given a weakly decrement of $< V_{TH} >$ with respect to $W$.

- For the $L_{eff}$ dependence: when $L_{eff}$ increases, the decrement of $\eta$ is strengthened by the decrement of $N_t$, given a strong decrement of $< V_{TH} >$ with respect to $W$. Note that this $L_{eff}$ dependence is the most important difference between CHC and BTI degradations.

In the temperature experiments, we have found that $\eta$ is independent of $T$ as in BTI degradation. As well, $N_t$ and $< V_{TH} >$ increase with respect to $T$ in agreement with the activation of the electron-electron scattering mechanism, which populates the tails of the carrier energy density function and enhances the defect generation. This increment of defects exhibits an activation energy of about 60mV, which coincides with BTI experiments.

Finally, we have studied the time-zero variability and the time-dependent variability. For the time-zero variability, we have showed that $V_{TH}$ and $\delta V_{TH0}$ follow a normal distribution up to $3\sigma$. As well, the $45nm$ technology exhibits more time-zero variability than the $65nm$ technology in agreement with the scaling rule $\sigma^2_{V_{TH0}} \propto 1/A_{eff}$. In the time-dependent variability experiments, we have shown that the total $\eta$ and the intrinsic $\eta$ are independent of $t_{stress}$ and $V_{Dstress}$. As well, we have found that the $45nm$ technology has more variability than the $65nm$ technology in concordance with the scaling rule $\eta \propto 1/A_{eff}$.

## 7.2 Future work

- In order to determine the percentage of interface traps, charge pumping experiments could be performed after each

stress time. This will enable us to confirm the basic theory that the interface states are predominant in CHC degradation.

- It would be very interesting to perform CHC experiments in high-$\kappa$ metal gate devices. In these devices, it would be necessary to separate the natural high density of oxide traps from those generated at the interface by the CHC stress.

- As well, It would be interesting to implement CHC experiments at high $T$ in high-$\kappa$ metal gate devices. In these devices the BTI component cannot be neglected and both degradations (CHC and BTI) will be present.

# Appendix A

# Activation Energy Conversion

According to experimental results, $< \Delta V_{TH} >$ follows a power law in function of $t_{stress}$. If we consider the temperature, the empirical rule can be written as:

$$< \Delta V_{TH} >= Kexp\left(\frac{-E_{ACT}}{k_B T}\right) t_{stress}^n, \quad (A.1)$$

where $K$ is a constant, $n$ is an exponent in the range $0.4 \sim 0.5$ for CHC experiments, and $E_{ACT}$ is the activation energy extracted from the typical curve $< \Delta V_{TH} >$ vs. $T$. With this equation, the stress time can be calculated by:

$$t_{stress} = \left( \frac{< \Delta V_{TH} >}{Kexp\left(\frac{-E_{ACT}}{k_B T}\right)} \right)^{\frac{1}{n}}. \tag{A.2}$$

One of the typical criterion for computing the failure time in CHC degradation is when a $< \Delta V_{TH} >= 30mV$ is obtained. If we replace this criterion in eq. (A.2), we have:

$$t_{failure} = \left( \frac{K_1}{Kexp\left(\frac{-E_{ACT}}{k_B T}\right)} \right)^{\frac{1}{n}}. \tag{A.3}$$

where $K_1 = 30mV$ and $t_{failure}$ is the failure time. Finally, we obtain:

$$t_{failure} = \left( \frac{K_1}{Kexp\left(\frac{-E_{ACT}}{k_B T}\right)} \right)^{\frac{1}{n}} = \left(\frac{K_1}{K}\right)^{\frac{1}{n}} exp\left(\frac{E_{ACT}}{k_B T}\right)^{\frac{1}{n}}, \tag{A.4}$$

$$log\left(t_{failure}\right) = \frac{1}{n} log\left(\frac{K_1}{K}\right) + \frac{E_{ACT}}{n}\frac{1}{k_B T}. \tag{A.5}$$

Therefore, $E_{A_{capture}} = \frac{E_{ACT}}{n}$. The relation of both activa-

tion energies is also explained in Fig. A.1.

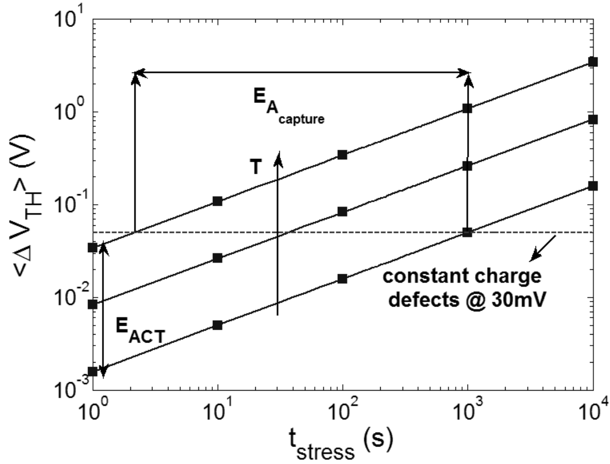


**Figure A.1:** In this simulated plot of $< \Delta V_{TH} >$ vs. $t_{stress}$, we can see the difference between both activation energies. In this case the exponent of the power law is 0.5.

# Appendix B

# Conversion between the Variances of Single Device Experiments and Matching Pairs Experiments

The mismatch of a parameter $X$, measured in MPD, is:

$$\delta X = X_A - X_B. \tag{B.1}$$

Then, the variance of $\delta X$ is:

$$var(\delta X) = var(X_A - X_B) = var(X_A) + var(X_B) - 2cov(X_A, X_B). \tag{B.2}$$

By considering that $X_A$ and $X_B$ are statistically independent and equally distributed, we have: $cov(X_A, X_B) = 0$ and $var(X_A) = var(X_B)$, therefore:

$$var(\delta X) = 2var(X_A) = 2var(X). \tag{B.3}$$

Finally,

$$var(X) = \frac{var(\delta X)}{2}. \tag{B.4}$$

# Bibliography

[1] C. Hu, *Lucky electron model for channel hot electron emission*, presented at IEEE Proceedings of the International Electron Devices Meeting (IEDM), pp. 22 - 25, 1979.

[2] S. Tam, P. K. Ko, and C. Hu, *Lucky-electron model of channel hot electron rejection in MOSFET'S*, IEEE Transactions on Electron Devices, vol. 31, pp. 1116 - 1125, 1984.

[3] C. Hu, S. C. Tam, F. C. Hsu, P. K. Ko, T. Y. Chan, K. W. Terril, *Hot-electron-induced MOSFET degradation-Model, monitor, and improvement*, IEEE Transactions on Electron Devices, vol. 32, pp. 375 - 385, 1985.

[4] S. Tyaginov, *Physics-Based Modeling of Hot-Carrier Degradation*, in Hot Carrier Degradation in Semiconductor Devices, 1st. ed. Switzerland.

[5] A. Bravaix, C. Guerin, V. Huard, D. Roy, J. M. Roux, E. Vincent, *Hot-Carrier acceleration factors for low power management in DC-AC stressed 40nm NMOS node at high temperature*, presented at IEEE International Reliability Physics Symposium (IRPS), pp. 531 - 548, 2009.

[6] E. Amat, T. Kauerauf, R. Degraeve, R. Rodriguez, M. Nafria, X. Aymerich, G. Groeseneken, *A comprehensive study of Channel Hot-Carrier degradation in short channel MOSFETs with high-k dielectrics*, Microelectronic Engineering, vol. 103, pp. 144 - 149, 2013.

[7] E. Amat, T. Kauerauf, R. Degraeve, R. Rodriguez, M. Nafria, X. Aymerich, G. Groeseneken, *Channel hot-carrier degradation in pMOS and nMOS short channel transistors with high-k dielectric stack*, Microelectronic Engineering, vol. 87, pp. 47 - 50, 2010.

[8] E. Amat, R. Rodríguez, M.B. González, J. Martín-Martínez, M. Nafría, X. Aymerich, P. Verheyen, E. Simoen, *CHC degradation of strained devices based on SiON and high-k gate dielectric materials*, Microelectronic Engineering, vol. 88, pp. 1408 - 1411, 2011.

[9] P. Magnone, F. Crupi, N. Wils, R. Jain, H. Tuinhout, P. Andricciola, G. Giusi, C. Fiegna, *Impact of Hot Carriers on nMOSFET Variability in 45 nm and 65 nm CMOS Technologies*, IEEE Transactions on Electron Devices, vol. 58, pp. 2347 - 2353, 2011.

[10] P. Magnone, F. Crupi, N. Wils, H. P. Tuinhout, C. Fiegna, *Characterization and Modeling of Hot Carrier-Induced Variability in Subthreshold Region*, IEEE Transactions on Electron Devices, vol. 59, pp. 2093 - 2099, 2012.

[11] M. Cho, Ph. Roussel, B. Kaczer, R. Degraeve, J. Franco, M. Aoulaiche, T. Chiarella, T. Kauerauf, N. Horiguchi, G. Groeseneken, *Channel Hot Carrier Degradation Mechanism in Long/Short Channel n-FinFETs*, IEEE Transactions on Electron Devices, vol. 60, pp. 4002 - 4007, 2013.

[12] S. E. Rauch, G. La Rosa, *The energy-driven paradigm of NMOSFET hot-carrier effects*, IEEE Transactions on Device and Materials Reliability, vol. 5, pp. 701 - 705, 2005.

[13] S. Tyaginov, M. Bina, J. Franco, Y. Wimmer, B. Kaczer, T. Grasser, *On the importance of electron-electron scattering for hot-carrier degradation*, Japanese Journal of Applied Physics, vol. 54, pp. 04DC18-1 - 04DC18-5, 2015.

[14] J. H. Sim, B. H. Lee, R. Choi, S.-C. Song, G. Bersuker, *Hot Carrier Degradation of HfSiON Gate Dielectrics With TiN Electrode*, IEEE Transactions on Device and Materials Reliability, vol. 5, pp 177 - 182, 2005.

[15] A. Tallarico, M. Cho, J. Franco, R. Ritzenthaler, M. Togo, N. Horiguchi, G. Groeseneken, F. Crupi, *Impact of the Substrate Orientation on CHC Reliability in n-FinFETs-Separation of the Various Contributions*, IEEE Transactions on Device and Materials Reliability, vol. 14, pp. 52 - 56, 2014.

[16] A. Bravaix, V. Huard, D. Goguenheim, E. Vincent, *Hot-carrier to cold-carrier device lifetime modeling with temperature for low power 40nm Si-bulk NMOS and PMOS FETs*, presented at IEEE International Electron Devices Meeting (IEDM), pp. 27.5.1 - 25.7.4, 2011.

[17] F. C. Hsu and K.-Y. Chu, *Temperature Dependence of Hot-Electron Induced Degradation in MOSFETs*, IEEE Electron Device Letters, vol. 5, pp. 148 - 150, 1984.

[18] M. Bina, S. Tyaginov, J. Franco, Y. Wimmer, D. Osinstev, B. Kaczer, T. Grasser, *Predictive Hot-Carrier Modeling of*

*n-channel MOSFETs*, IEEE Transactions on Electron Devices, vol. 61, pp. 3103 - 3110, 2014.

[19] B. Kaczer, T. Grasser, Ph. J. Roussel, J. Franco, R. Degraeve, L.-A. Ragnarsson, E. Simoen, G. Groeseneken, H. Reisinger, *Origin of BTI Variability in Deeply Scaled pFETs*, presented at IEEE International Reliability Physics Symposium (IRPS), pp. 26 - 32, 2010.

[20] B. Kaczer, Ph. J. Roussel, T. Grasser, G. Groeseneken, *Statistics of Multiple Trapped Charges in the Gate Oxide of Deeply Scaled MOSFET Devices-Application to BTI*, IEEE Electron Device Letters, vol. 31, pp. 411 - 413, 2010.

[21] M. Toledano-Luque, B. Kaczer, J. Franco, Ph.J. Roussel, M. Bina, T. Grasser, M. Cho, P. Weckx, and G. Groeseneken, *Degradation of time dependent variability due to interface state generation*, presented at Symposium on VLSI Technology (VLSIT), pp. T190 - T191, 2013.

[22] D. Angot, V. Huard, L. Rahhal, A. Cros, X. Federspiel, A. Bajolet, Y. Carminati, M. Saliva, E. Pion, F. Cacho, A. Bravaix, *BTI variability Fundamental understandings and Impact on digital logic by the use of extensive dataset*,

presented at IEEE International Electron Devices Meeting (IEDM), pp. 15.4.1 - 15.4.4, 2013.

[23] C. Prasad, M. Agostinelli, J. Hicks, S. Ramey, C. Auth, K. Mistry, S. Natarajan, P. Packan, I. Post, S. Bodapati, M. Giles, S. Gupta, S. Mudanai, *Bias Temperature Instability Variation on SiON/Poly, HK/MG and Trigate Architectures*, presented at IEEE International Reliability Physics Symposium (IRPS), pp. 6A.5.1 - 6A.5.7, 2014.

[24] E. R. Hsieh, Steve S. Chung, C. H. Tsai, R. M. Huang, C. T. Tsai, C. W. Liang, *New Observations on the Physical Mechanism of Vth-Variation in Nanoscale CMOS Devices After Long Term Stress*, presented at IEEE International Reliability Physics Symposium (IRPS), pp. XT.9.1 - XT.9.2, 2011.

[25] S. S. Chung, *The Process and Stress-Induced Variability Issues of Trigate CMOS Devices*, presented at IEEE International Conference of Electron Devices and Solid-State Circuits (EDSSC), pp. 1 - 2, 2013.

[26] C.H. Tu, S.Y. Chen, A.E. Chuang, H.S. Huang, Z.W. Jhou, C.J. Chang, S. Chou, J. Ko, *Transistor variability after*

*CHC and BTI stress in 90 nm pMOSFET technology*, Electronics Letters, vol. 45, pp. 854 - 856, 2009.

[27] C. Liu, K. T. Lee, S. Pae, and J. Park, *New Observations on Hot Carrier induced Dynamic Variation in Nano-scaled SiON/Poly, HK/MG and FinFET devices based on On-the-fly HCI Technique: The Role of Single Trap induced Degradation*, presented at IEEE International Electron Devices Meeting (IEDM), pp. 34.6.1 - 34.6.4, 2014.

[28] I. A. Starkov, S.E. Tyaginov, H. Enichlmair, J. Cervenka, Ch. Jungemann, S. Carniello, J.M. Park, H. Ceric, T. Grasser, *Hot-carrier degradation caused interface state profile - simulations vs. experiment*, Journal of Vacuum Science & Technology B, vol. 29, pp. 01AB09-1 - 01AB09-8, 2011.

[29] I. Starkov, H. Enichlmair, S. Tyaginov, T. Grasser, *Analysis of the threshold voltage turnaround effect in high-voltage n-MOSFETs due to hot-carrier stress*, presented at IEEE International Reliability Physics Symposium (IRPS), pp. XT.7.1 - XT.7.6, 2012.

[30] W. McMahon, K. Matsuda, J. Lee, K. Hess, J. Lyding, *The effects of a multiple carrier model of interface states gen-*

*eration of lifetime extraction for MOSFETs*, presented at Proceedings of the International Conference on Modelling and Simulation Micro, vol. 1, pp. 576 - 579, 2002.

[31] W. McMahon, A. Haggag, K. Hess, *Reliability scaling issues for nanoscale devices*, IEEE Transaction on Nanotechnology, vol. 2, pp. 33 - 38, 2003.

[32] K. Hess, L.F. Register, B. Tuttle, J. Lyding, I.C. Kizilyalli, *Impact of nanostructure research on conventional solid-state electronics: The giant isotope effect in hydrogen desorption and CMOS lifetime*, Physica E, vol. 3, pp. 1 - 7, 1998.

[33] S. E. Rauch, G. La Rosa, F.J. Guarin, *Role of E-E scattering in the enhancement of channel hot carrier degradation of deep-submicron NMOSFETs at high Vgs conditions*, IEEE Transactions on Device and Materials Reliability vol. 1, pp. 113 - 119, 2001.

[34] S. Rauch, G. La Rosa, *The energy driven paradigm of NMOSFET hot carrier effects*, presented at IEEE International Reliability Physics Symposium (IRPS)International Reliability Physics Symposium (IRPS), pp. 708 - 709, 2005.

[35] S. Rauch, F. Guarin, G. La Rosa, *Impact of E-E Scatering to the Hot Carrier Degradation n Deep Submicron NMOSFETs*, IEEE Electron Device Letters, vol. 19, pp. 463 - 465, 1998.

[36] C. Guerin, V. Huard, A. Bravaix, *General framework about defect creation at the Si/SiO2 interface*, Journal of Applied Physics, vol. 105, pp. 114513-1 - 114513-12, 2009.

[37] C. Guerin, V. Huard, A. Bravaix, *The energy-driven hot-carrier degradation modes of nMOSFETs*, IEEE Transactions on Device and Materials Reliability, vol. 7, pp. 225 - 235, 2007.

[38] C. Guerin, V. Huard, A. Bravaix, *The energy-driven hot carrier degradation modes*, presented at IEEE Proceedings of the International Reliability Physics Symposium (IRPS), pp. 692 - 693, 2007.

[39] A. Bravaix, V. Huard, D. Goguenheim, E. Vincent, *Hot-carrier to cold-carrier device lifetime modeling with temperature for low power 40nm Si-Bulk NMOS and PMOS FETs*, presented at IEEE International Electron Devices Meeting (IEDM), pp. 622 - 625, 2011.

[40] Y. M. Randriamihaja, X. Federspiel, V. Huard, A. Bravaix, P. Palestri, *New hot carrier degradation modeling reconsidering the role of EES in ultra short n-channel MOSFETs*, presented at IEEE Proceedings of the International Reliability Physics Symposium (IRPS), pp. 1 - 5, 2013.

[41] M. Aoulaiche, *Bias temperature instabilities in MOSFETs with high-k dielectrics and metal gates*, Ph.D. dissertation, Departement Elektrotechnieka, Katholieke Universiteit Leuven, Leuven, Belgium, 2009.

[42] M. F. Bukhori, S. Roy, and A. Asenov, *Simulation of statistical aspects of reliability in nano CMOS*, presented at IEEE International Integrated Reliability Workshop (IRW), pp. 82 - 85, 2009.

[43] A. Ghetti, C. M. Compagnoni, A. S. Spinelli, A. Visconti,, *Comprehensive analysis of random telegraph noise instability and its scaling in deca-nanometer Flash memories*, IEEE Transactions on Electron Devices, vol. 56, pp. 1746 - 1752, 2009.

[44] M. Toledano-Luque, B. Kaczer, J. Franco, Ph.J. Roussel, T. Grasser, G. Groeseneken, *Defect-centric perspective of*

*time-dependent BTI variability*, Microelectronics Reliability, vol. 52, pp. 1883 - 1890, 2012.

[45] S. E. Rauch, *Review and reexamination of reliability effects related to NBTI statistical variations*, IEEE Transactions on Device and Materials Reliability, vol. 7, pp. 524 - 530, 2017.

[46] V. Huard, C. Parthasarathy, C. Guerin, T. Valentin, E. Pion, M. Mammasse, N. Planes, L. Camus, *NBTI degradation: From transistor to SRAM arrays*, presented at IEEE Proceedings of the International Reliability Physics Symposium (IRPS), pp. 289 - 300, 2008.

[47] B. Kaczer, T. Grasser, J. Martin-Martinez, E. Simoen, M. Aoulaiche, P. J. Roussel, and G. Groeseneken, *NBTI from the perspective of defect states with widely distributed times*, presented at IEEE Proceedings of the International Reliability Physics Symposium (IRPS), pp. 55 - 60, 2009.

[48] T. Kauerauf, *Degradation and breakdown of MOS gate stacks with high permittivity dielectrics*, Ph.D. dissertation, Departement Elektrotechnieka, Katholieke Universiteit Leuven, Leuven, Belgium, 2007.

[49] L. M. Procel, F. Crupi, J. Franco, L. Trojman, B. Kaczer, *Defect-Centric Distribution of Channel Hot Carrier Degradation in Nano-MOSFETs*, IEEE Electron Device Letters, vol. 35, pp. 1167 - 1169, 2014.

[50] L. M. Procel, F. Crupi, J. Franco, L. Trojman, B. Kaczer, N. Wils, H. Tuinhout, *A Defect-Centric perspective on channel hot carrier variability in nMOSFETs*, Microelectronic Engineering, vol. 147, pp. 72 - 74, 2015.

[51] J. Franco, B. Kaczer, M. Toledano-Luque, Ph. J. Roussel, J. Mitard, L.-A. Ragnarsson, L. Witters, T. Chiarella, M. Togo, N. Horiguchi, G. Groeseneken, *Impact of Single Charged Gate Oxide Defects on the Performance and Scaling of Nanoscaled FETs*, presented at IEEE Proceedings of International Reliability Physics Symposium (IRPS), pp. 5A.4.1 - 5A.4.6, 2012.

[52] M. Toledano-Luque, B. Kaczer, T. Grasser, P. Roussel, J. Franco, G. Groeseneken, *From mean values to distributions of BTI lifetime of deeply scaled FETs through atomistic understanding of the degradation*, presented at Symposium on VLSI Technology (VLSIT), pp. 152 - 153, 2011.

[53] M. Toledano-Luque, B. Kaczer, J. Franco, Ph.J. Roussel, T. Grasser, T.Y. Hoffmann, G. Groeseneken, *Toward a streamlined projection of small device BTI lifetime distributions*, Journal of Vacuum Science and Technology B, vol. 31, pp. 01A114, 2013.

[54] J. Franco, B. Kaczer, Ph. J. Roussel, M. Toledano-Luque, P. Weckx, *Relevance of non-exponential single-defect-induced threshold voltage shifts for NBTI Variability*, presented at IEEE International Integrated Reliability Workshop (IRW), pp. 69 - 72, 2013.

[55] B. Kaczer, J. Franco, M. Cho, T. Grasser, Ph. J. Roussel, S. Tyaginov, M. Bina, Y. Wimmer, L. M. Procel, L. Trojman, F. Crupi, G. Pitner, V. Putcha, P. Weckx, E. Bury, Z. Ji, A. De Keersgieter, T. Chiarella, N. Horiguchi1, G. Groeseneken, A. Thean, *Origins and Implications of Increased Channel Hot Carrier Variability in nFinFETs*, presented at IEEE International Reliability Physics Symposium (IRPS), pp. 3B.5.1 - 3B.5.6, 2015.

[56] B. Kaczer, J. Franco, Ph. J. Roussel, G. Groeseneken, T. Chiarella, N. Horiguchi, T. Grasser, *Extraction of The Random Component of Time-Dependent Variability Using*

*Matched Pairs*, IEEE Electron Device Letters, vol. 36, pp. 300 - 302, 2015.

[57] T. Mizutani, A. Kumar, T. Hiramoto, *Analysis of transistor characteristics in distribution tails beyond* $\pm 5.4\sigma$ *of 11 billion transistors*, presented at IEEE International Electron Devices Meeting (IEDM), pp. 33.3.1 - 33.3.4, 2013.

[58] M. J. M. Pelgrom, A. C. J. Duinmaijer, A. P. G. Welbers, *Matching Properties of MOS Transistors*, IEEE Journal of Solid-State Circuits, vol. 24, pp. 1433 - 1439, 1989.

[59] C. M. Mezzomo, A. Bajolet, A. Cathignol, R. Di Frenza, G. Ghibaudo, *Characterization and Modeling of Transistor Variability in Advanced CMOS Technologies*, IEEE Transactions on Electron Devices, vol. 58, pp. 2235 - 2248, 2011.

[60] A. Kerber, *Methodology for Determination of Process Induced BTI Variability in MG/HK CMOS Technologies Using a Novel Matrix Test Structure*, IEEE Electron Device Letters, vol. 35, pp. 294 - 296, 2014.